



Deep versus shallow emplacement of sills and dykes: new insight from thermo-visco-elastic modelling

Harro Schmeling^{*}, Gernold Zulauf

Institute of Geosciences, Goethe University Frankfurt, Germany (H.S. retired)

ARTICLE INFO

Keywords:

Dykes and Sills
Magma emplacement
Physics of magma and magma bodies
Sederholm-type vein
Weschnitz pluton
Visco-elastic stress relaxation

ABSTRACT

Rapid emplacement of a mafic dyke or sill at mid-crustal depth heats and possibly melts the felsic wall rock followed by solidification. Associated volume changes generate stresses, possibly enforcing brittle failure and melt migration. We model the evolution of melting, solidification, temperature, and stress including visco-elastic relaxation in 1D - dykes or -sills using realistic rock rheologies of the Weschnitz pluton (Odenwald). For deep emplacement (Case 1, 15.3 km) extensive contact melting of the wall rock occurs, for shallow emplacement (Case 2, 10 km) it is negligible. The stresses are zero at high melt fractions, but increase during solidification and cooling: The intrusion orthogonal stress is always zero. The intrusion parallel stress σ_{\parallel} within the intrusion is tensile (O(200 MPa)). It relaxes on a time scale between a few years (Case 1) and 0.6 m.y. (Case 2). Within the wall rock σ_{\parallel} is compressive during heating, but becomes tensile under solidification and cooling. Wall rock stresses relax on a time scale of months to 100 years. A Deborah number is defined based on viscous to thermal relaxation allowing generalization of our results. Adding lithostatic stresses, the total stresses of Case 1 remain below the brittle strength, while for Case 2 they may exceed it. Adding the lithostatic pressure to the melt pressure, the effective stresses exceed the brittle strength and intrusion orthogonal tensile fractures are predicted. Combined with the pressure gradient within the over-pressurized felsic melts generated in the wall rock, this explains the migration of felsic contact melt into shrinkage cracks of the mafic sill in the Weschnitz pluton.

1. Introduction

The trajectory of sheeted intrusions like dykes and sills is controlled by the orientation of the principal stresses, while their propagation depends on the temperature and buoyancy of the melt, the magma pressure, the wall rock temperature, and the ambient tectonic stress field (Rivalta et al., 2015, and references therein; Maccaferri et al., 2019). As these parameters vary in space and time and result in a large range of combined physical and chemical processes occurring within sheeted intrusions, the mechanics of their formation and propagation is still a matter of debate. For dyke formation, three mechanical models have been suggested, all of which are highly simplified with respect to actual dykes in nature (Rivalta et al., 2015 and references therein; Townsend et al., 2017; Fig. 1): (1) A certain amount of magma buoyantly flows within a vertical fracture that migrates upward by closing at its lower tip and opening at its upper tip (Dahm, 2000). (2) Upward flow of magma is controlled by pressure from a distant source and opens fracture at its upper tip. (3) Magma migrates horizontally in a vertical fracture that opens, but maintains its height and position, while loaded by static stress

and pressure gradients due to gravity. Whatever the mode of emplacement, the magma cools, solidifies, but also heats up the ambient rock (Gudmundson, 1990; Turcotte and Schubert, 2002; Petcovic and Dufek, 2005). Depending on the initial temperature of the ambient rock, the heating may also lead to partial melting of the host rock (e.g., Sederholm, 1907, 1912; Eskola, 1960; Litvinovsky et al., 2012; Zulauf et al., 2021). Alternatively, multiple emplacement events through the same sill or dyke may melt the ambient rock (Petcovic and Grunder, 2003; Petcovic and Dufek, 2005). Upon cooling and solidification, shrinkage of the intruded material and thermal expansion of the ambient rock modify the stress field, leading to features observable by the structural geologist in the field (e.g. Litvinovsky et al., 2017; Zulauf et al., 2021). Depending on the depth and mode of emplacement, such features include (1) shrinkage cracks of mafic sheets are filled with felsic melt derived from the wall rock (Figs. 1a,b; Zulauf et al., 2021 and references therein), or (2) sill- and dyke-parallel and -orthogonal joints (Figs. 1c,f), (3) chilled margins (Fig. 1d), and (4) dyke-orthogonal basalt columns in shallow intrusions (Fig. 1e).

During solidification and subsequent cooling, the viscosity of the

^{*} Corresponding author.

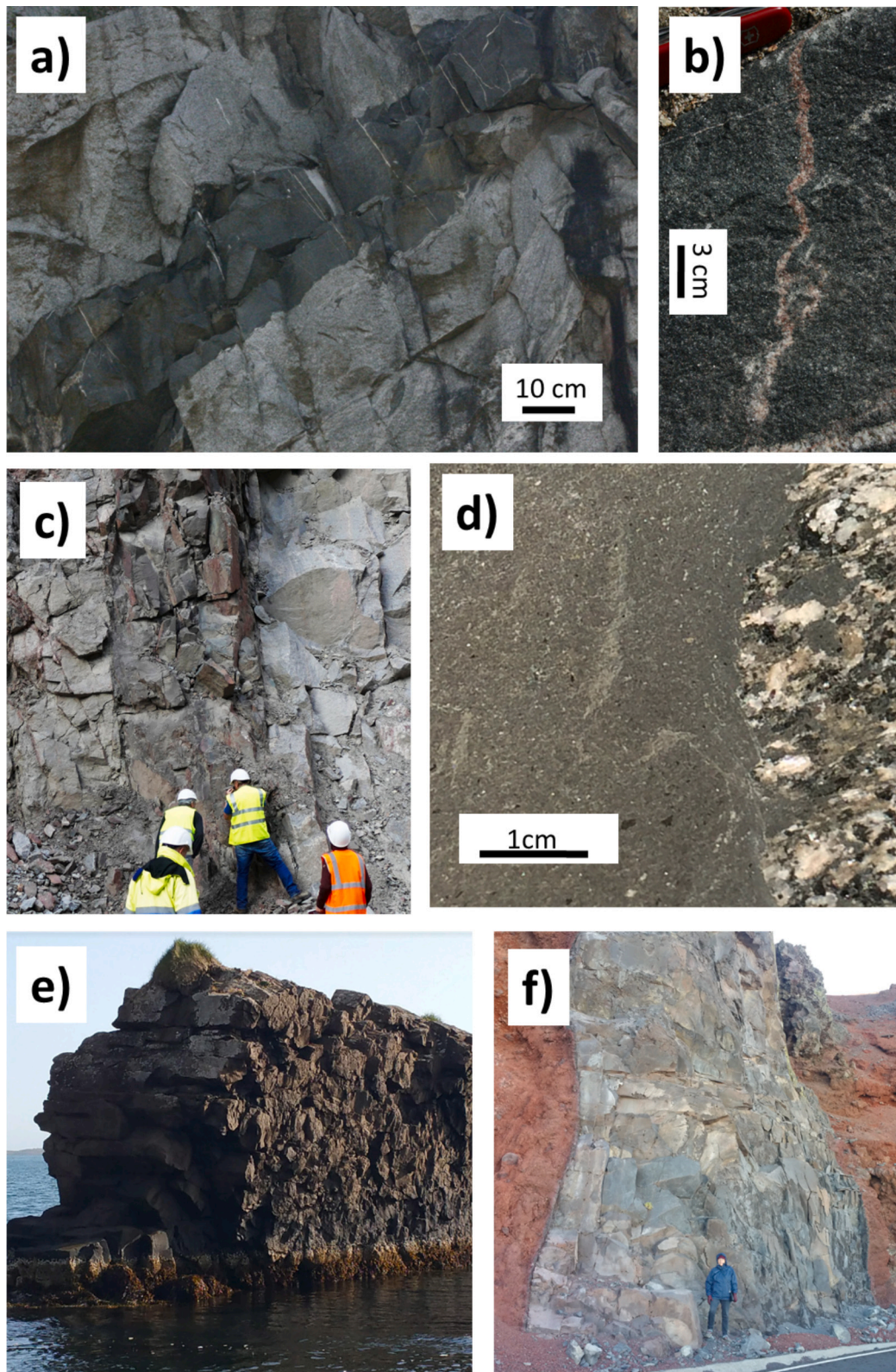


Fig. 1. Examples of deep and shallow dykes and sills. a) Spessartite sill, which cuts through quartzmonzodiorite of the Weschnitz pluton, Odenwald. Emplacement depth was about 15 km (Zulauf et al., 2021). Note thin felsic veins inside the spessartite. b) Felsic vein within the spessartite sill originating from the quartzmonzodiorite host. c) Vein-parallel and -orthogonal cracks in spessartite dyke, which cuts through quartzmonzodiorite host at the same location as in a), but at shallower depth of about 10 km and ca. 8 million years later (von Seckendorff et al., 2004). d) Photograph of fractured surface showing the chilled margin of the dyke depicted in c). e) Vertical shallow dyke emplaced at a maximum depth of 1.3–1.5 km below the original, pre-erosional surface (Walker, 1974) of the Tertiary Basalt Formation in East Iceland. Note the dyke-orthogonal cracks and basalt columns. f) Shallow dyke (< 800 m below original volcano surface, Carracedo and Troll (2016)) cutting through scoria beds in Caldera del Taburiente, La Palma. Note the dyke-parallel and orthogonal cracks.

intrusion rapidly increases by many orders of magnitude, while the viscosity of the adjacent host rock first decreases during heating and possible partial contact melting, but subsequently increases as cooling progresses. Together with the elastic properties of the solid and solidified rocks, the system behaves in a visco-elastic manner. Depending on the involved viscous relaxation times, cooling stresses may build up or may be relaxed. Given the effective elasticity of rock, such stresses are related to fluid pressure in the melt whose gradient may drive porous melt flow. See e.g. [Turcotte and Schubert \(2002\)](#) for these processes and the associated rock behavior. Several of the processes related to this scenario have been modelled separately in previous numerical approaches:

Thermal modelling approaches of a dyke and its wall rock go back to the 1950's, e.g. by [Jaeger \(1957\)](#), and have been followed up by many others, e.g. [Irvine \(1970\)](#), [Delany and Pollard \(1982\)](#), [Zulauf and Helfferich \(1997\)](#), and [Petecovic and Dufek \(2005\)](#). In the latter study, the solidification of basaltic magma and melting of the wall rock have been modelled for both an instantaneously injected dyke and a dyke undergoing continuous melt in- and outflux. Thermal modelling approaches on sill formation can also be found in a series of papers e.g. by [Annen et al. \(2006\)](#). They modelled multiple injections of mafic sills by solving the 1D heat equation with a FD resolution larger than the thickness of each intruded sill. [Solano et al. \(2012\)](#) extended the 1D-injection models by accounting for the mass conservation due to magma injection and allowing for melt segregation within the partially molten layer. Multiple injections of circular sills with various diameters have been used to build up an axisymmetric crustal magma chamber ([Annen et al., 2008](#)). Focusing on a planar intrusion, [Annen \(2017\)](#) solved the 1D heat equation analytically and numerically to study the thickness of aureoles relative to the thickness of the intrusion. This thickness ratio strongly depends on the thermal diffusivity contrast between the intrusion and wall rock, and on whether single or multiple intrusion events have taken place. In all these approaches, thermal stresses or visco-elasticity has not been considered.

Important issues are the stresses and strains associated with the magmatic intrusions. The width of emplaced tabular dykes and sills of finite radius within an elastic medium due to magma over-pressure has been determined by [Gudmundsson \(1990\)](#). To determine elastic stresses induced by over-pressurized magma of dykes and sills near discontinuities, numerical modelling (e.g. Finite Elements as in the COMSOL-package) is necessary (e.g. [Barnett and Gudmundsson, 2014](#)). Such modelling showed that the arrest of dykes strongly depends on layer stiffness and thickness contrasts of the emplacement region ([Drymoni et al., 2020](#); [Bazargan and Gudmundsson, 2019](#)). In these studies stresses were assumed being due to magmatic over-pressure rather than of thermal origin.

Focusing on magma chambers, pressurization due to magma influx leads to effects such as dyke initiation and deformation of the ambient crust and earth surface uplift (e.g. [Suppe, 1983](#); [Pinel and Jaupart, 2003](#); [Karlstrom et al., 2010](#)). Thermal, elastic and visco-elastic modelling has been invoked to study such magma emplacement processes. Elastic stresses around a pressurized ellipsoidal magma chamber in a rift zone may be used to determine dyke initiation at the top of the magma chamber ([Gudmundsson, 2006](#)). [Jellinek and DePaolo \(2003\)](#) embedded a spherical magma chamber in a visco-elastic half-space to determine the conditions for initiating dykes. Visco-elastic stress and pressure relaxation within a circular over-pressurized magma chamber and outside of it have been determined by [Karlstrom et al. \(2010\)](#) using the Laplace transform for Maxwell rheology. To model the crustal response to the time-dependent pressurization of a spherical or ellipsoidal magma chamber in a visco-elastic medium with Standard Linear Solid (SLS) or Maxwell rheology, Laplace transformations and Finite Element modelling have been used ([Hickey et al., 2013, 2016](#); [Liao et al., 2023](#); [Rucker et al., 2022](#)). [Head et al. \(2019\)](#) systematically tested three visco-elastic configurations, namely Maxwell, SLS, and Kelvin-Voigt. They favor the SLS for volcanic surface deformations because of the least irreversible

strain. In all these elastic or visco-elastic approaches magma chambers rather than tabular intrusions have been considered, and the loading mechanism was mostly magma chamber pressurization rather than thermal stresses.

Focusing on magma transport through the crust and emplacement, [Karlstrom et al. \(2009, 2017\)](#) modelled propagating dykes constrained by buoyancy and ambient stresses generated by magma bodies, volcanic edifices and dykes. They include the effect of large-scale heating and visco-elasticity to distinguish between viscous ($De < 1$) and elastic ($De > 1$) regimes in the crust, where De is the Deborah number. Visco-elastic relaxation has been determined averaged on the large scale in terms of fluid over-pressure. Multiple stochastic dyke intrusions initiated at the Moho control the thermal and compositional evolution of the lower crust ([Karakas and Dufek, 2015](#)) and may lead to flow, mixing, and mingling on crustal scale ([Dufek and Bergantz, 2005](#)). Compared to these studies, our approach focuses on the small scale of a single dyke or sill intrusion.

Thermal stresses in volcanic environments such as those due to thermal expansion of magma bodies contribute to the stress field around magma chambers and the surface as has been modelled in crustal-scale thermo-mechanical purely elastic 2D Finite Elements models by [Browning et al. \(2021\)](#). In laboratory experiments, [Browning et al. \(2016\)](#) studied small-scale heating- and cooling-induced cracking of volcanic rocks at room pressure. Cooling-induced acoustic emissions were much higher than during heating. Thermal cracking may lead to damage reducing the elastic moduli and strength of the cooled rock. In these experiments expansion and contraction was probably close to isotropic, while here we will address the effect of heating and cooling on deviatoric stresses and fluid pressure.

The effect of thermal contraction of a cooling sill has been modelled by [Aarnes et al. \(2009\)](#). They used a simplified isochoric (constant volume) condition to calculate the pressure. A negative pressure gradient was found from the center of the intrusion towards the solidifying contact zone. From this, they predict small amounts of melt migration towards the contact zone. Compared to their approach, we will invoke visco-elasticity, solidification induced stresses, non-isochoric conditions for calculating the fluid pressure, and emphasize the potential of brittle fracturing.

The aim of this paper is to quantitatively explore the post-emplacement stress build-up of a cooling, visco-elastic, planar intrusion embedded in an initially cold host rock, which may undergo partial contact melting or not. Two cases will be distinguished: Case 1 represents deep emplacement with contact melting, Case 2 shallow emplacement with negligible contact melting. The resulting melt pressure and potential brittle failure will be estimated. Non-dimensionalization will be applied to generalize the findings. At least the dykes modelled in the present paper were not related to a local stress field near a magma chamber ([Nickel and Fettel, 1985](#)), but were opened due to extensional tectonic stresses, which may trigger dyke emplacement ([Gudmundsson, 2006](#)).

2. Model setup and governing equations

2.1. Thermal and partial melting approach

We assume that a sill or dyke of width h and an initial temperature $T_{i0} = 1050$ °C has intruded into an ambient host rock at about 15 km depth having a temperature $T_{a0} = 650$ °C (Case 1, [Fig. 1a](#)) or 400 °C (Case 2, [Fig. 1c](#)). For simplicity, constant, but possibly different thermal parameters are assumed for the intrusion and wall rock ([Table 1](#)). As boundary condition, symmetry is chosen at $x = 0$ at the center of the intrusion, and at the side of the model domain the temperature is fixed at 650 °C for Case 1 or 400 °C for Case 2. As in [Zulauf et al. \(2021\)](#), the dyke is assumed to represent a spessartite intrusion within a quartz-monzodiorite pluton at 15 km depth for Case 1 or 10 km depth for Case 2. Assuming a planar intrusion with infinite extension, the problem can

Table 1

Symbols, their definition, numerical values, and physical units used in this study. Subscripts i and a refer to intrusion and ambient rock, respectively.

Symbol	Definition	Value intrusion	Value ambient rock	Units
A	Pre-factor in the rheology law of Kirby and Kronenberg (1987)	$2 \cdot 10^{-4}$	$1.26 \cdot 10^{-9}$	$\text{MPa}^n \text{s}^{-1}$
B	Skempton coefficient (pore pressure / ambient pressure)	variable	variable	–
c_p	Specific heat capacity	1100	1100	$\text{J kg}^{-1} \text{K}^{-1}$
d	Grain size (Case 1)	$3 \cdot 10^{-4}$	$2 \cdot 10^{-3}$	m
De, De_{cool}	Deborah number (general), De based on cooling time scale	variable	variable	–
E_a	Activation energy	$260 \cdot 10^3$	$106 \cdot 10^3$	J mol^{-1}
E_0	Young's modulus of unmolten rock	$0.7 \cdot 10^{11}$	$0.7 \cdot 10^{11}$	Pa
E	Effective Young's modulus of partially molten rock ($=E_0$ for unmolten rock)	variable	variable	Pa
e_{ij}, e	Elastic strain tensor, dilatational unconstrained strain, $e = \frac{1}{3} \frac{\Delta V}{V}$	variable	variable	–
e_1, e_2, e_3	Principal elastic strains	variable	variable	–
e_{\parallel}, e_{\perp}	Intrusion parallel and orthogonal strain, respectively	variable	variable	–
$\dot{e}_1^v, \dot{e}_2^v, \dot{e}_3^v$	Principal viscous strain rates	variable	variable	s^{-1}
$\dot{e}_1^{tot}, \dot{e}_2^{tot}, \dot{e}_3^{tot}$	Total principal visco-elastic strain rates	variable	variable	s^{-1}
h_i, h_a	Width of intrusion and wall rock in Case 1 (Case 2)	0.4 (2)	2 (10)	m
k_i, k_a	Thermal conductivity	1.6	1.5	$\text{W m}^{-1} \text{K}^{-1}$
k_p	Permeability of partially molten rock	variable		m^2
K_0	Bulk modulus of solid rock	$0.466 \cdot 10^{11}$	$0.466 \cdot 10^{11}$	Pa
K_d	Dry bulk modulus of rock with empty pores	variable	variable	Pa
K_s	Effective bulk modulus of rock saturated with melt	variable	variable	Pa
L_i, L_a	Latent heat	400	400	kJ/kg
n_i, n_a	Stress exponent	3.4	2.9	–
P	Pressure	variable	variable	Pa
P_f	Fluid pressure of the melt without lithostatic pressure	variable	variable	Pa
$P_{f_{tot}}$	Fluid pressure of the melt including lithostatic pressure			
R	Gas constant	8.31		$\text{J mol}^{-1} \text{K}^{-1}$
$t, \Delta t$	Time, time step	variable	variable	s
t_{max}	Maxwell time	variable	variable	s
T	Temperature	variable		$^{\circ}\text{C}$
T_{si}, T_{sa}	Solidus temperature	800	680	$^{\circ}\text{C}$
T_{li}, T_{la}	Liquidus temperature	1000	970	$^{\circ}\text{C}$
$V, \Delta V$	Volume, stress-free volume change	–	–	m^3
x	Coordinate orthogonal to the planar intrusion	–	–	m
y, z	Coordinates parallel to the planar intrusion	–	–	m
α	Thermal expansivity	$3 \cdot 10^{-5}$	$3 \cdot 10^{-5}$	K^{-1}
α_l	Linear thermal expansivity	10^{-5}	10^{-5}	K^{-1}
α_i	Aspect ratio of ellipsoidal melt inclusions	0.2	0.2	–
β_f	Melt compressibility	0.037	0.037	GPa^{-1}
β_p	Formation compressibility, function of φ	$10^{-9} - 10^{-10}$	$3 \cdot 10^{-9} - 3 \cdot 10^{-10}$	GPa^{-1}
δ_{ij}	Kronecker symbol, = 1 if $i = j$, else = 0			–

Table 1 (continued)

Symbol	Definition	Value intrusion	Value ambient rock	Units
η_b	Effective bulk viscosity of the porous matrix	variable	variable	Pa s
η_b'	Porosity dependent bulk viscosity, scaled by η_{sol}	variable	Variable	–
η_E	Elongational (Young's) viscosity of the porous matrix	variable	variable	Pa s
η_s	Effective shear viscosity of the porous matrix	variable	variable	Pa s
η_{sol}	Intrinsic shear viscosity of the solid	variable	variable	Pa s
η_f	Melt viscosity	$10 - 10^3$	10^4	Pa s
η_p'	Porosity dependent shear viscosity, scaled by η_{sol}	variable	variable	–
κ_p	Pore pressure diffusivity	0.005–2.3	0.007–0.8	$\text{m}^2 \text{s}^{-1}$
μ_0	Shear modulus of solid rock	$0.233 \cdot 10^{11}$	$0.233 \cdot 10^{11}$	Pa
μ_r	Effective low frequency shear modulus of partially molten rock	variable	variable	Pa
ν_0	Poisson ratio of unmolten rock	0.25	0.25	–
ν	Effective Poisson ratio of partially molten rock ($=\nu_0$ for unmolten rock)			
ν_{η}	Viscous Poisson ratio	variable	variable	–
ρ_i, ρ_a	Solid density	2900	2800	kg m^{-3}
ρ_f, ρ_{fa}	Density of fluid phase (i.e. melt)	2500	2400	kg m^{-3}
ρ_{si}, ρ_{sa}	Density of solid rock	2900	2800	kg m^{-3}
$\Delta\rho$	Density difference between solid and melt $=\rho_s - \rho_f$	400	400	kg m^{-3}
σ_{ij}	Stress tensor	variable	variable	Pa
$\sigma_1, \sigma_2, \sigma_3$	Principal stresses, tension positive, compression negative, ($\sigma_1 \geq \sigma_2 \geq \sigma_3$),	variable	variable	Pa
$\sigma_1', \sigma_2', \sigma_3'$	Principal stresses in tectonic sign convention, compression positive, tension negative, ($\sigma_1' \geq \sigma_2' \geq \sigma_3'$)	variable	variable	Pa
$\sigma_{1eff}, \sigma_{3eff}$	First and third effective principal stress, reduced by pore pressure	variable	variable	Pa
σ_N', σ_T'	Normal, tangential (shear) stress on a plane of certain orientation with respect to σ_1' , tectonic sign convention	variable	variable	MPa
$\sigma_{\parallel}, \sigma_{\perp}$	Intrusion parallel and orthogonal normal stresses, respectively. Tension positive, compression negative	variable	variable	Pa
σ_0'	Lithostatic stress of Case 1 (Case 2)	420 (280)	420 (280)	MPa
τ_{ij}	Viscous stress tensor in the solid phase	variable	variable	Pa
τ_{II}	Second invariant of the viscous stress tensor	variable	variable	Pa
φ	Volumetric melt porosity (i. e. melt fraction)	variable	variable	–

be described in 1D by the heat equation

$$\rho c_p \frac{\partial T}{\partial t} = k \frac{\partial^2 T}{\partial x^2} - \rho L \frac{\partial \varphi}{\partial t} \quad (1)$$

with ρ as density, c_p as specific heat capacity, k as thermal conductivity, L as latent heat or enthalpy per mass due to melting (positive, therefore the minus sign), and φ as melt fraction or melt porosity (these terms are used synonymously within this paper, implying that the pore space is completely filled with melt). We assume batch melting, thus there exist melting curves for $\varphi(T)$ for the intrusion and the wall rock (Fig. 2b). For

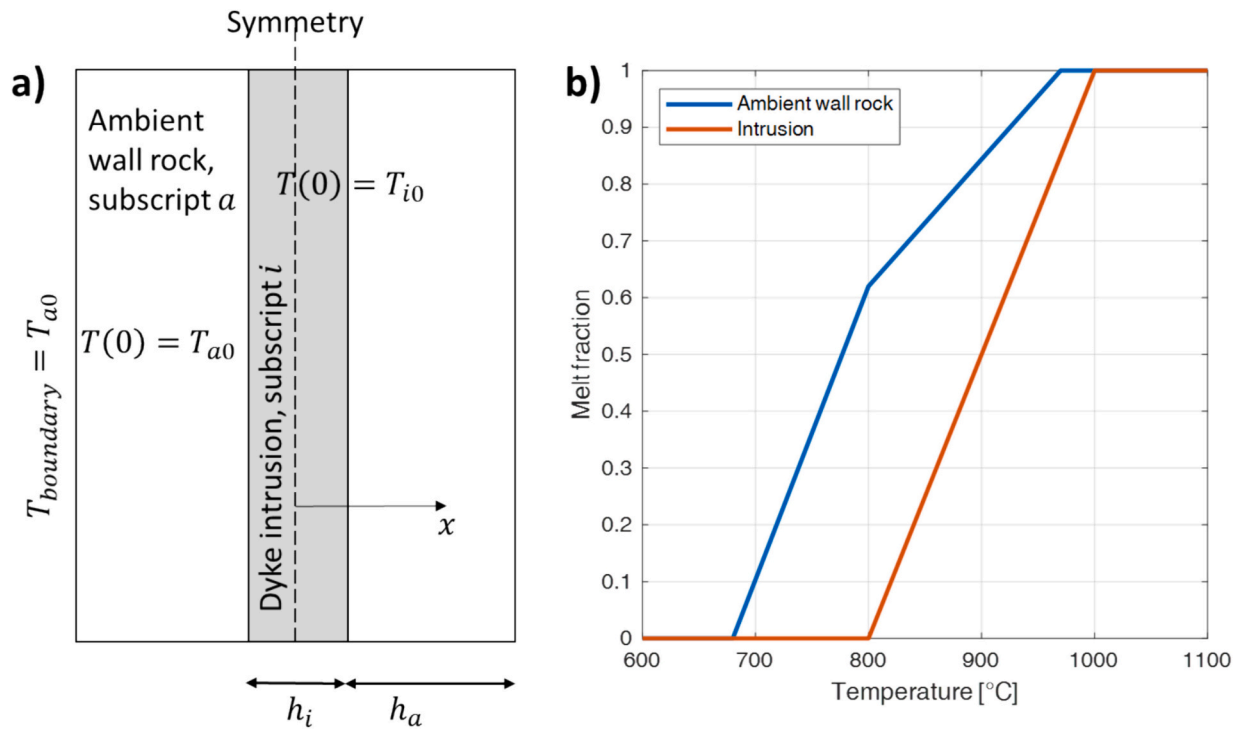


Fig. 2. a) Model setup, b) Assumed melt laws for the intrusion and ambient wall rock.

the wall rock, we approximate data from Costa et al. (2004) for dacite, which is expected to be close to quartzmonzodiorite. For the intrusion, the solidus and liquidus temperatures are taken for wet gabbro and spessartite, respectively (Lambert and Wyllie, 1972; Moore and Carmichael, 1998). The melting curve is assumed as a linearly increasing function between the solidus and liquidus temperatures (Fig. 2b). With these melting curves we replace the last term of eq. (1) by $\frac{\partial \varphi}{\partial t} = \frac{\partial \varphi}{\partial T} \frac{\partial T}{\partial t}$ and obtain (see e.g. Annen, 2017)

$$\rho c_{peff} \frac{\partial T}{\partial t} = k \frac{\partial^2 T}{\partial x^2} \quad (2)$$

with

$$c_{peff} = c_p + L \frac{\partial \varphi}{\partial T} \quad (3)$$

As there do not exist analytical solutions of eqs. (2) and (3) including the release of latent heat according to specific melting laws, the equations are solved in 1D by Finite Elements using the software package COMSOL with the parameters given in Table 1. The spatial resolution was 5.5 mm (30 mm for Case 2) and quadratic shape functions were used. The output times were chosen logarithmically between 100 s and 10^8 s (i.e. about 3 years) or between 2500 s and $2.5 \cdot 10^9$ s for Case 2.

2.2. Elastic approach

The stress evolution of the system will be investigated due to thermal contraction and solidification of the intrusion material as well as due to melting and solidification of the ambient rock. Other sources of stresses such as vertical lithostatic stress, horizontal non-lithostatic stresses, stresses associated with the process of intrusion (dyke propagation, sill emplacement) or other tectonic stresses will not be considered here and may be superimposed to the stresses of the sill or dyke appropriately if desired. In this paper, we mostly use the physics stress notation, i.e. tensile normal stress is positive, compressive normal stress is negative. Wherever needed (e.g. in section 5.1), the tectonic sign notation will be used by using primed stress components (see also Table 1). First, the

purely elastic 1D case will be considered. Embedding an infinite planar elastic inclusion into an infinite medium a volume change of the inclusion is applied due to thermal or phase change contraction. Solidification related contraction will generate elastic stresses only below the ‘melt connectivity transition’ (Rosenberg and Handy, 2005) or the ‘rheological critical melt percentage’ (RCMP), which is of the order of 20% melt (Arzi, 1978). The RCMP depends on the melt geometry. From the discussion in Weinberg et al. (2021) it is expected that the RCMP lies between 12 and 36% for granite. The theory of an elastic ellipsoidal inclusion (Eshelby, 1957) can be used to derive the elastic stress due to contraction within the inclusion and outside. The planar elastic inclusion is assumed to lie parallel to the sill or dyke in the yz -plane. An unconfined volume change $\frac{\Delta V}{V}$ is applied to this inclusion. If confined within an infinite elastic medium of the same elastic properties, the stress within the inclusion is given by (see Supporting information S1)

$$\sigma_{\parallel} \equiv \sigma_{yy} = \sigma_{zz} = -\frac{E}{1-\nu} \frac{1}{3} \frac{\Delta V}{V} \quad (4)$$

$$\sigma_{\perp} \equiv \sigma_{xx} = 0 \quad (5)$$

where E and ν are the Young’s modulus and Poisson ratio, respectively, and the inclusion parallel and orthogonal directions are indicated by the subscripts \parallel, \perp , respectively. Thus, cooling and related shrinkage generates sill- or dyke-parallel (positive) tensile stresses. An infinite planar intrusion does not experience an intrusion orthogonal stress. In fact the finite contraction in x -direction (perpendicular to the dyke or sill) pulls the ambient medium towards the intrusion without generating external stress. The ambient half spaces on both sides distribute their strains to infinite distances so that they vanish. Furthermore, from the solution found in Supporting information S1 (eq. 6), there is no intrusion-parallel strain within the intrusion, nor at the interface. From continuity of displacements it follows that the ambient medium is also strain-free and therefore stress-free in y - and z -direction. Remember, this is only the case immediately after volume change within the elastic layer. Due to thermal evolution, the ambient rock will experience heating or cooling stresses later, which can be described in 1D by eq. (4) by using

appropriate thermal expansion or contraction volume changes.

As in this 1D-problem no deviatoric stresses or strains occur, the normal stresses and strains are principal stresses and strains. Note, that in our problem, the stress magnitudes vary and the signs may change. From eq. (4) and (5) and from Supporting information S1 we summarize the elastic response of an infinite elastic layer undergoing a volume change as

$$\sigma_{\parallel} = -\frac{E}{1-\nu} \frac{\Delta V}{3V}, \quad \sigma_{\perp} = 0, \quad e_{\parallel} = 0, \quad e_{\perp} = \frac{1+\nu}{1-\nu} \frac{\Delta V}{3V} \quad (6)$$

One important result is that only e_{\perp} (intrusion orthogonal) is non-zero. Thus, the problem is in the state of *uni-axial strain*, i.e. only one normal strain component is non-zero, the other two are zero, while normal stresses may be non-zero in more than one component. This is an important result because it will allow combining elasticity with viscous behavior (see below). While eq. (6) is the solution inside the layer, the ambient medium is stress- and strain-free (see Supporting information S1). Remember, $\frac{\Delta V}{V}$ is the stress free thermal or phase change related volume change. Eq. (6) states that such a volume change does not lead to any strain in layer-parallel direction. Due to the Poisson effect, the layer-parallel tensile stresses σ_{\parallel} lead to some thinning of the intrusion associated with the strain e_{\perp} . Thus, the constrained volume change $\left(\frac{\Delta V}{V}\right)_{constr} = e_{xx} + e_{yy} + e_{zz} = 2e_{\parallel} + e_{\perp} = \frac{1+\nu}{1-\nu} \frac{\Delta V}{3V}$, i.e. it is smaller than the unconstrained volume change by a factor of about 5/9 for a typical rock Poisson ratio of 0.25. Finally, it should be noted that due to linear elasticity and the assumption of 1D, the elastic solution (eq. 6) could be extended to any infinitesimal layer in the yz - plane within or outside the dyke or sill. For x -dependent temperatures, such solutions can simply be superimposed.

2.3. Visco-elastic constitutive law

We now construct a visco-elastic constitutive law for a cooling and solidifying planar intrusion in a cold host rock. It is reasonable to extend the previous result of the state of *uni-axial strain* also to visco-elastic behavior. Following Turcotte and Schubert (2002), we formulate the visco-elastic problem including volume changes by combining the three principal strain – stress equations for elasticity with those for viscous behavior. In our problem the principal directions are identical to the x, y , and z - directions. As we will use laboratory based steady state viscosities in our visco-elastic formulation, Maxwell rheology will be assumed rather than the Standard Linear Solid (Head et al., 2019) which is more representative for short term processes such as seismic waves attenuation. This means, stresses are the same in the viscous and elastic elements, but strains add up. First, we derive the viscous constitutive law for the partial molten solid, i.e. for the solid or partially molten rock below the RCMP. We allow viscous compaction or decompaction. Taking the equivalent Hooke's law for the viscous strain rate for the stress – strain relation in z -direction parallel to the intrusion one can write

$$\dot{e}_{zz}^v = \frac{1}{\eta_E} \sigma_{zz} - \frac{\nu_{\eta}}{\eta_E} (\sigma_{xx} + \sigma_{yy}) \quad (7)$$

with η_E and ν_{η} as the viscous Young's modulus (elongational viscosity) and viscous Poisson ratio of the (porous) solid. Assuming a viscously compressible or compacting porous (partially molten) solid and using standard elastic modulus relations, this can be written in terms of effective bulk and shear viscosity (see Table 1 for the definitions):

$$\dot{e}_{zz}^v = \frac{3\eta_b + \eta_s}{9\eta_b\eta_s} \sigma_{zz} - \frac{3\eta_b - 2\eta_s}{18\eta_b\eta_s} (\sigma_{xx} + \sigma_{yy}) \quad (8)$$

Outside of the partially molten region the solid is viscously incompressible, $\eta_b = \infty$ (Schmeling et al., 2012), and we get

$$\dot{e}_{zz}^v = \frac{1}{3\eta_s} \sigma_{zz} - \frac{1}{6\eta_s} (\sigma_{yy} + \sigma_{xx}) \quad (9)$$

For this region, it can easily be verified that this equation is equivalent to the standard viscous constitutive law

$$\dot{e}_{zz}^v = \frac{1}{2\eta_s} \tau_{zz} \quad (10)$$

where τ_{zz} is the normal deviatoric stress in parallel direction. Furthermore, the volumetric viscous strain rate, $\dot{e}_{xx}^v + \dot{e}_{yy}^v + \dot{e}_{zz}^v$ is equal to zero, i.e. \dot{e}_{zz}^v is equal to the deviatoric strain rate.

Now we construct the visco-elastic constitutive law by adding up the elastic, viscous, thermal and phase change induced strains due to melting or solidification. Note, that the elastic strains of the solution (6) is valid only as an initial condition, and elastic strains and stresses will depart from this solution as stresses relax. We take Hooke's law for the elastic strains including volumetric strains due to thermal and phase changes, take their first time derivative (denoted by the dot) to get the elastic and volumetric strain rates, add the viscous strain rate (8) and obtain the total normal strain rate in z - direction:

$$\dot{e}_{zz}^{tot} = \frac{\dot{\sigma}_{zz}}{E} - \frac{\nu}{E} (\dot{\sigma}_{xx} + \dot{\sigma}_{yy}) + \frac{3\eta_b + \eta_s}{9\eta_b\eta_s} \sigma_{zz} - \frac{3\eta_b - 2\eta_s}{18\eta_b\eta_s} (\sigma_{xx} + \sigma_{yy}) + \alpha_I \dot{T} + \frac{\Delta\rho}{3\rho_0} \dot{\phi} \quad (11)$$

\dot{e}_{xx}^{tot} and \dot{e}_{yy}^{tot} can be written by permutation of the stress and strain indices. Here α_i is the linear coefficient of thermal expansion with $\alpha_i = \frac{1}{3}\alpha$ where α is the volumetric coefficient of expansion, $\frac{\Delta\rho}{\rho_0}$ is the relative density change between solid and melt, i.e. $\Delta\rho = \rho_s - \rho_f$ with the subscripts s and f for solid and fluid (melt), respectively. One third of this volume change acts in each direction, therefore the 3 in the last term of eq. (11), where $\dot{\phi}$ is the rate of change of melt fraction. Given an infinite intrusion in the yz -plane, we may assume uni-axial strain, i.e. $\dot{e}_{yy}^{tot} = \dot{e}_{xx}^{tot} = 0$. The assumption of total uniaxial strain implies that during viscous relaxation the elastic and viscous strains in z - and y -direction (intrusion parallel) will be non-zero, only the total strains are zero. As the zero stress condition in x -direction (intrusion orthogonal) still holds under visco-elastic relaxation, we have $\sigma_{yy} = \sigma_{zz} = \sigma_{\parallel}$ and $\sigma_{xx} = \sigma_{\perp} = 0$, thus the pressure is given as

$$P = -\frac{1}{3} (\sigma_{xx} + \sigma_{yy} + \sigma_{zz}) = -\frac{2}{3} \sigma_{\parallel} \quad (12)$$

With $\dot{e}_{zz}^{tot} = 0$ eq. (11) gives (replacing the indices zz by the intrusion parallel subscript \parallel)

$$0 = \frac{1-\nu}{E} \dot{\sigma}_{\parallel} + \frac{3\eta_b + 4\eta_s}{18\eta_b\eta_s} \sigma_{\parallel} + \frac{1}{3} \alpha_I \dot{T} + \frac{\Delta\rho}{3\rho_0} \dot{\phi} \quad (13)$$

This first order inhomogeneous ordinary differential equation is the visco-elastic constitutive law for the stress (or, with eq. (12), the pressure) in intrusion parallel (y or z) direction. It can be solved subject to the initial condition for the stress. As initial condition we use $\sigma_{\parallel}(t=0) = 0$ as the intrusion is completely molten (i.e. above the RCMP) and the solid ambient rock is still at initial temperature. From section 4.1 we obtain the temperature and melt fraction as functions of x and t . Using these solutions, eq. (13) can be integrated in time for each value of x . No coupling between different x -positions occurs because of the *uni-axial strain* condition. In the following we drop the indices xx, yy , and zz , and replace them by either \parallel or \perp depending on whether we consider intrusion parallel or orthogonal stresses. For example, $\sigma_{\parallel}(x)$ is the normal stress in any intrusion parallel direction. The numerical scheme for solving eq. (13) is described in the Supporting information (S2).

2.4. Effective elasticity, rheology and melt pressure

In eq. (13) the elastic parameters E, ν of the rock are not constant but

depend on the melt fraction. Here we use the self-consistent elastic composite formulation given in Schmeling (1985). Approximate formulas for the elastic moduli as a function of melt fraction are derived in the Supporting information (S3), assuming an aspect ratio of 0.2 for the melt inclusions.

For the shear viscosity of the solid, a stress- and temperature - dependent viscosity is taken for both the intrusion and ambient rock (see details in the Supporting information S3). Rheological parameters are taken from Kirby and Kronenberg (1987) for diabase representing the intrusion (sill or dyke), and for Westerly granite representing the ambient rock (Table 1). In the presence of melt, the effective viscosity of the rock drops further. The viscosity-dependence on melt fraction is taken from Schmeling et al. (2012) with details given in Supporting information S3. The melt fraction leading to compete disaggregation of the partially molten rock depends on the melt geometry and is identified with the rheological critical melt percentages (RCMP). In our model, we choose the aspect ratio 0.2 for effective melt inclusions leading to a RCMP of 31.3%.

At finite melt fraction, the melt is assumed to be connected. Thus, any lateral variations of pore pressure will equilibrate by porous flow on a time scale short compared to solidification (Supporting information S3). In the presence of melt, we distinguish between two cases:

1) In the case where at some position the melt fraction exceeds the RCMP, the melt can be regarded as drained and the melt pressure and the stress $\sigma_{||}$ are zero.

2) In the case that the melt fraction is below the RCMP everywhere, volume changes due to freezing or melting contribute to the stress change as a response to freezing or melting.

Although the melt pressure is assumed to equilibrate rapidly in our approach, it is interesting to estimate the instantaneous, undrained melt pressure as this melt pressure drives porous melt flow. This instantaneous melt pressure is determined by using the Skempton coefficient (Bagdassarov, 2022; see Supporting information S3).

3. Geological setup of the tested cases

To test our model, we use the Variscan Weschnitz pluton (Odenwald) as a natural laboratory. This pluton belongs to a Carboniferous magmatic arc (Altherr et al., 1999) and was cut by mafic (spessartite) sills and dykes at different times and different structural levels. In the total alkalis vs. SiO₂ (TAS) diagram, the investigated sill and dyke plot at the transition from trachybasalt to basaltic trachyandesite (Zulauf et al., 2021; Fig. 7). The formation of the parent melt was probably related to partial melting of metasomatized mantle due to lithosphere detachment, removal and replacement of metasomatized lithospheric mantle by upwelling hot asthenospheric mantle (von Seckendorff et al., 2004). The wall rock consists of quartzmonzodiorite, which intruded at 344.3 ± 0.6 Ma (U—Pb on zircon, Zulauf et al., 2021) at a depth of 18.2 ± 1.5 km (Al-in-hornblende barometry, Altherr et al., 1999). After a short period of exhumation and cooling (< 3.9 m.y.), the quartzmonzodiorite attained its solidus (ca. 680 °C) and was cut by a ca. 40 cm thick spessartite sill (Case 1) at 342 ± 1 Ma (U—Pb on titanite) at a depth of 15.3 ± 1.1 km (Al-in-hornblende barometry, Zulauf et al., 2021). The sill itself is cut by Sederholm-type shrinkage cracks, which are filled with felsic contact melt derived from the adjacent partially molten wall rock (Figs. 1a and b). The age of these felsic veins (341.8 ± 1.5 Ma, U—Pb on titanite, Zulauf et al., 2021) is the same like that of the spessartite sill. Apart from partial contact melting, sill emplacement did not cause a metamorphic overprint of the adjacent quartzmonzodiorite. However, bulk vertical constriction at still high temperature (ca. 660 °C) led to prolate grain shape fabrics, mullions along the contact sill/wall rock, and boudinage of the felsic veins within the sill (Zulauf et al., 2022).

Further cooling of the Weschnitz pluton to $T = \text{ca. } 500$ °C and 300 °C (the closure temperatures of the K—Ar system of amphibole and biotite, respectively (Harrison, 1981; Harrison et al., 1985)) was relatively slow. K—Ar dating of hornblende and of biotite yielded 333 ± 4 and 325 ± 4

Ma, respectively (Kreuzer and Harre, 1975, recalculated). These ages are consistent with ³⁹Ar—⁴⁰Ar dating of hornblende and biotite, which yielded ca. 333 and ca. 329 Ma (Rittmann, 1984). ³⁹Ar—⁴⁰Ar dating of hornblende of a NNE-SSW trending, ca. 2 m thick spessartite dyke (Case 2) yielded a plateau age at 334 ± 4 Ma (von Seckendorff et al., 2004), which is similar to that of the wall rock. Compared to the sill, the dyke is much finer in grain size and displays a chilled margin (Fig. 1d). A dyke-related metamorphic overprint of the adjacent quartzmonzodiorite is lacking. For this reason, the ³⁹Ar—⁴⁰Ar age is interpreted as emplacement age. Thus, the dyke intruded ca. 8 million years later than the sill. Apart from dyke-parallel and -orthogonal joints (Fig. 1c), the dyke is largely undeformed. The depth of intrusion and the temperature of the wall rock during dyke emplacement are less well constrained compared to those of the sill. Based on a weak greenschist-facies overprint along the margins of the dyke and the thermal constraints resulting from the K—Ar and ³⁹Ar—⁴⁰Ar ages of hornblende and biotite, it is concluded that the dyke emplaced under greenschist-facies conditions (ca. 400 °C) at a depth of ca. 10 km.

4. Results

4.1. Thermal and partial melt evolution of a solidifying sill or dyke

In Fig. 3a, b, the thermal evolution and the evolution of the melt fraction are shown for the instantaneous intrusion of a molten sill or dyke into a 650 °C warm host rock (Case 1). This solution is identical to that shown in Zulauf et al. (2021, Fig. 13). However, here a different visualization has been chosen to better elucidate the mutual temporal evolutions of temperature and melt fraction within and outside the intrusion.

For the first 1000 s, the central part of the intrusion remains fully molten. Only latent heat is lost essentially from its edge into the wall rock. It should be noted that in our configuration of Case 1 the total heat is almost equally partitioned into latent heat 400 kJ/kg and sensible heat $(T_{i0} - T_{a0})c_{pi} = 440$ kJ/kg. A thermal boundary layer develops (thin curve) and penetrates into the host rock following the square root time law $h_{th} = 2.32\sqrt{\kappa_a t}$ with κ_a as thermal diffusivity of the ambient rock and the value 2.32 chosen as to mark the distance up to which 90% of the thermal disturbance has penetrated (Turcotte and Schubert, 2002). After about 1000 s, the intrusion starts solidifying from the contact zone, the melt fraction drops from 100% and reaches zero at the center of the intrusion after a few days. During this phase, more and more latent heat is lost until all melt in the intrusion has solidified. Thus, the square root of time law is a good approximation here during this early stage up to about a day. Further cooling continues until after several months most of the sensible heat is lost in the wall rock far away ($> > 2$ m) from the intrusion.

As the wall rock heats up between 10^5 and 10^6 s (few days to a month), it reaches its maximum temperature, with a delay further away from the intrusion. As the melting law of the host rock is below that of the intrusion (c.f. Fig. 2b), the host rock progressively melts, while the intrusion freezes. During the early phase, the melt fraction reaches about 70% close to the contact zone. This stems from the early temperature at the contact zone, which is about $T_{a0} + \frac{(T_{i0} - T_{a0})}{2} = 850$ °C. This temperature is higher than the solidus temperature of both the host rock (680 °C) and the intrusion (800 °C). As heating of the host rock continues, the melting front penetrates deeper and deeper up to about 1.2 m, or about 2.5 intrusion widths, from the contact zone. During this stage, the intrusion is already fully solidified. The maximum extent of both the thermal disturbance (almost 2 m) and partial melting (ca. 1.3 m) is present in the wall rock after about 1 month. It takes until 10^7 s (several months) until also the host rock is fully solidified.

An important finding for Case 1 is that for a rather long time, up to $3 \cdot 10^5$ s, the intrusion and the host rock are both simultaneously partially molten, i.e. melt may percolate through that zone in either direction

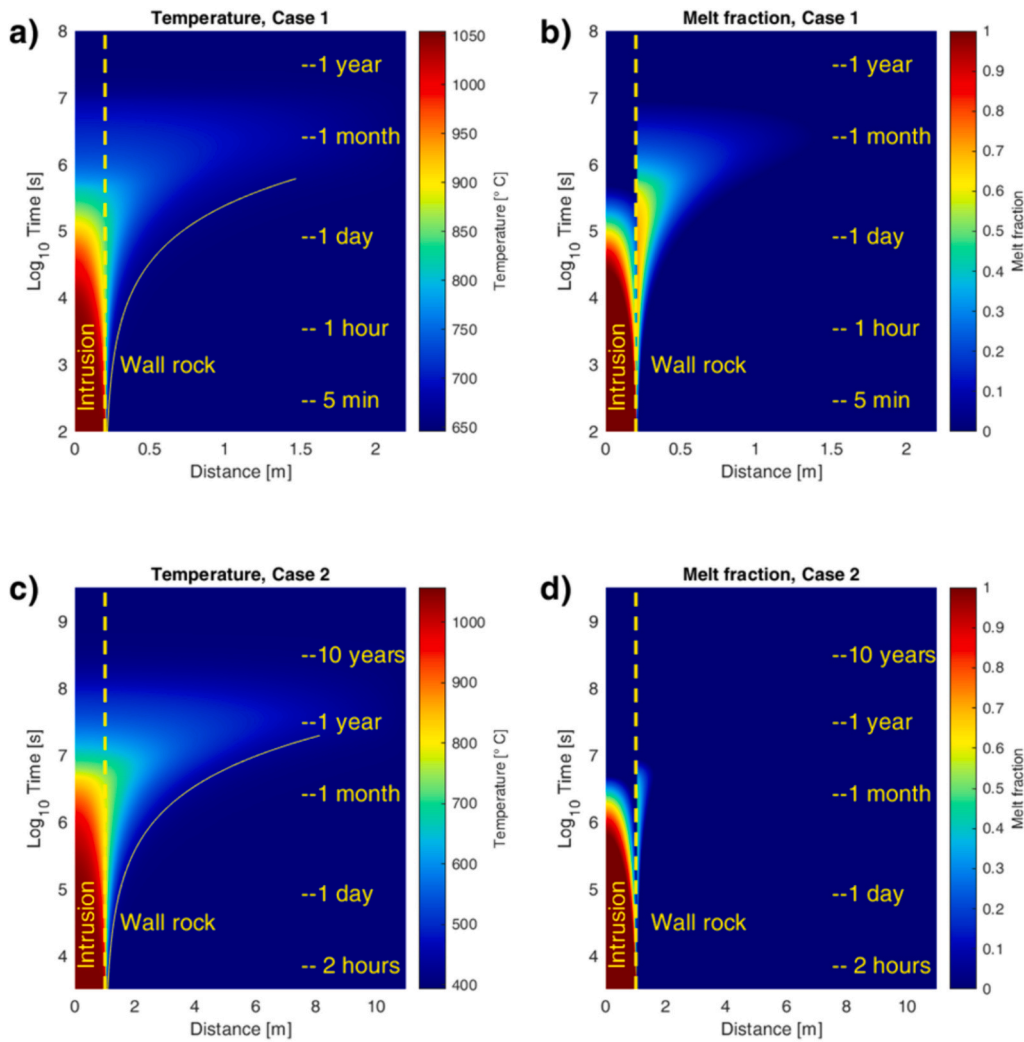


Fig. 3. a) Case 1: Thermal evolution after emplacement of a 0.4 m wide dyke or sill with initial temperature 1050 °C into a wall rock with initial temperature of 650 °C. The logarithmic time progresses upwards, some time steps are explicitly indicated. Only the right half of the symmetric vein and wall rock is shown. The thin curve shows the evolution of the thermal boundary layer in the host. b) Case 1: Evolution of melt fraction. c) Case 2: As a) but with a 2 m wide dyke intrusion into a 400 °C warm wall rock. d) Case 2: Evolution of melt fraction. The dashed lines indicate the contact between the intrusion and the wall rock.

depending on the lateral fluid pressure gradient. This stems from the fact that the early temperature at the contact zone is above the solidus for both materials. Moreover, a large amount of partial melt is present in the wall rock, while the intrusion undergoes a considerable change in viscosity by freezing. Note that this will be different for Case 2 described below.

Summarizing the results for Case 1 so far, the thermal evolutions inside and outside the intrusion are characterized by a diffusively widening of the thermal anomaly. However, the melting and solidification evolution of the host rock is significantly delayed with respect to the occurrence of melt within the intrusion. Given typical volume changes due to solidification and cooling, this delay will have important consequences for the evolution of the stress field, as well as for the viscous relaxation of such stresses (see next section).

While in Case 1 migration of contact melt into shrinkage cracks of the cooling sill is expected, we now test Case 2) of a shallower dyke intruded at 10 km depth in which a) the host rock is colder (400 °C) and b) the dyke is 5 times wider (2 m) (Fig. 1c). Assuming all other parameters the same (c.f. Table 1), Figs. 3c and d show the thermal and melt evolution. As the thermal diffusion time scales with the square of the characteristic length (intrusion width), a similar thermal evolution is obtained, but on a time scale 25 times longer than in Case 1. Due to the logarithmic time scale, Fig. 3c is very similar to Fig. 3a, but all features are shifted to later

times by almost 1.5 decades. As a result, complete cooling lasts about 10 years. The temperature at the contact interface is about $400 \text{ °C} + (1050 \text{ °C} - 400 \text{ °C})/2 = 725 \text{ °C}$, i.e. it is only moderately above the solidus temperature of the host rock, but 75 °C below the solidus of the intrusion. This explains the formation of a chilled margin, which is entirely lacking in the sill of Case 1. Thus, despite of contact melting, from the beginning there is a solid impermeable layer between the dyke and host rock inhibiting melt exchange between the two rocks. Remember, in Case 1 the contact temperature was above the solidus for both the intrusion and ambient rock. Due to colder ambient temperature in Case 2, only small ambient rock melt fractions, mostly below the RCMP (rheological critical melt percentage, see section 3.1) are visible over a much shorter relative distance (Fig. 3d) than in Case 1 (Fig. 3b). The maximum extent of the thermal disturbance (almost 10 m) and of the zone of partial melting (ca. 1.5 m) in the wall rock occurs after about 1 year and 2 month, respectively. Similar to Case 1, it takes several months until the host rock attains a fully solid state.

4.2. Stress evolution due to cooling and solidification

In this section we first present the evolution of the intrusion-parallel stress, σ_{\parallel} , of an instantaneously intruded sill or dyke into a 15 km deep pluton as discussed above and in Zulauf et al. (2021) (Case 1), and as

resulting from our visco-elastic approach (Fig. 4a, b). This evolution is complemented by the temporal evolution of the effective shear viscosity of the rock (Fig. 4c) and the Maxwell relaxation time (Fig. 4d). This Maxwell time is valid for uni-axial strain ($e_{yy} = e_{zz} = 0, e_{xx} \neq 0$) within an elastic and viscously compressible medium. It can be derived directly from the homogeneous part of the differential eq. (13) giving

$$t_{mxw} = \frac{6(1-\nu)}{E} \frac{\eta_s}{1 + \frac{4}{3} \frac{\eta_s}{\eta_b}} \quad (14)$$

For fully solidified rock ($\eta_b = \infty$) this Maxwell time reduces to

$$t_{mxw} = \frac{6\eta_s(1-\nu)}{E} \quad (15)$$

which is about 1.8 times longer than the Maxwell time for shear deformation (η_s/μ) with μ as shear modulus. The stress evolution should be evaluated together with the thermal and melt evolution shown and discussed above (Fig. 3). Immediately after intrusion of the 1050 °C hot melt into the host rock of 650 °C, e.g. after 100 to 1000 s, the intrusion is still almost completely molten. Only within a very thin thermal boundary layer (of order 1 to 5 cm) in the intrusion near the contact zone to the wall rock at $x = 0.2$ m the intruded melt is cooled down to the intermediate temperature 850 °C. This intermediate temperature is maintained up to 10,000 s to 30,000 s until the thermal boundary layer reaches the center of the sill. At that temperature, the melt fraction within the sill or dyke is only slightly below the RCMP (31%). The intrusion is practically free of deviatoric stress ($\sigma_{||} = 0$). On the wall rock side of the contact zone, a similar thermal boundary layer forms with a melt fraction mostly above the RCMP, i.e. free of deviatoric stress, while outside of the thermal boundary layer the wall rock is still at initial temperature, i.e. also free of deviatoric stress. Within a narrow layer

between the molten and the still ‘cold’ wall rock e.g. at $x = 0.2143$ m, thermal expansion generates compressive stress increasing from 0 to -80 MPa (narrow dark blue band in Fig. 4a and yellow dashed curve in Fig. 4b).

After about 1000 s, the wall rock continues to heat up and to melt, and the compressive region (dark blue band) broadens and penetrates deeper into the wall rock (Fig. 4a). At that time, the wall rock partially melts near the sill or dyke. At the contact zone, the wall rock is above the RCMP, which is associated with zero deviatoric stress (light blue region widening until 10^6 s). In the darker blue region the melt fraction is below the RCMP, only thermal stresses due to heating, no expansion related melting stresses, contribute to the compressive stress $\sigma_{||}$ because melt is drained. The stress curve at $x = 0.2143$ m drops back to 0 because at that position the melt fraction exceeds the RCMP (Fig. 4b, see also Fig. 3b).

Once the cooling of the sill or dyke leads to a melt fraction below the RCMP at $x = 0.1978$ m and 10^5 s near the contact zone or at the center ($x = 0$ m) at about $2 \cdot 10^5$ s, cooling generates intrusion-parallel tensile stresses $\sigma_{||} > 0$ (green to yellow zone within the intrusion in Fig. 4a and red and blue curve in Fig. 4b, respectively). These stresses are predominantly of thermal, not freezing origin because even below the RCMP within the sill or dyke the melt is assumed to be connected with the partially molten region of the wall rock, which is still above the RCMP. After about $4 \cdot 10^5$ s the intrusion is completely frozen (Fig. 3b) and continues to cool. The tensile stress increases further until about $2 \cdot 10^7$ s, when viscous relaxation takes over and stresses start to relax (Fig. 4a, red curve in Fig. 4b).

Focusing on the ambient rock, the melt fraction drops below the RCMP at about 10^6 s (Fig. 3b), i.e. later than within the intrusion. At that instance, the melt is no more drained by a region with high melt fraction. It continuously freezes within the partially molten zone between 0.2 and 1.4 m between 10^6 and 10^7 s (Fig. 3b). This freezing contributes to the

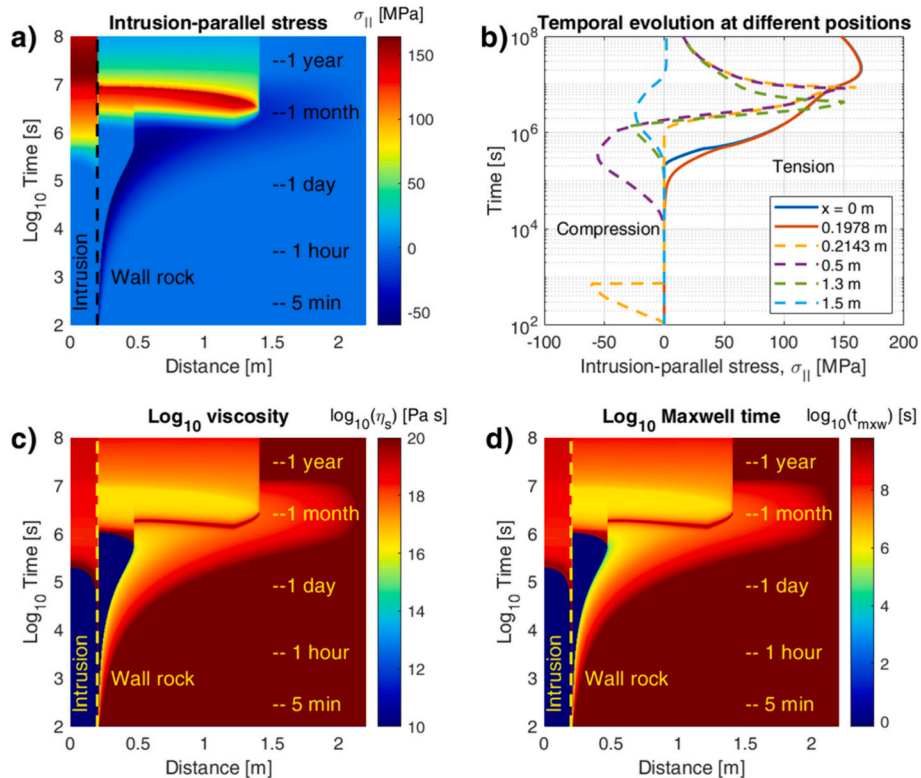


Fig. 4. Case 1: Evolution of intrusion-parallel normal stress $\sigma_{||}$ (a and b), viscosity (c), and Maxwell time (d) of a planar intrusion and ambient wall rock due to cooling, heating, melting, solidification, and visco-elastic relaxation. Tensile and compressive stresses are indicated by positive and negative sign, respectively. The thermal and melt fraction evolution is the same as for the model shown in Fig. 3. In b) the solid curves represent intrusion-parallel normal stresses within the intrusion, while the dashed curves show the stresses within the ambient rock at the indicated positions. The intrusion-ambient rock contact is at $x = 0.2$ m (vertical dashed lines).

strong build-up of intrusion-parallel tensile stresses $\sigma_{\parallel} > 0$ due to phase change induced contraction (green to yellow to red zone in Fig. 4a, rapidly increasing yellow, purple and green dashed curves in Fig. 4b). Once the freezing comes to the end, the phase change driven contraction rate (last term in eq. 11) becomes zero. The tensile stress in the wall rock first relaxes relatively rapidly (red to yellow zone in Fig. 4a, over-exponential dropping of green, yellow and purple curves in Fig. 4b), then more slowly. This is related to a rapid increase in shear viscosity (Fig. 4c) because a) no more weakening by melt is present and b) the stress dependent viscosity increases as the stress decreases. The increase of viscosity leads to a subsequent increase of the Maxwell time (Fig. 4d). In fact, during the freezing stage, the Maxwell time is of the order of 10^6 s, which is an order of magnitude shorter than the total time needed for freezing. Thus, only a short visco-elastic delay occurs during freezing. At the end of freezing, stresses relax on a time scale of 10^7 to 10^8 s, i.e. some of the freezing and cooling stresses are still stored in the rock and relax slowly on time scales of several years. The time-dependence of the Maxwell time is the reason for the over-exponential decay of the stresses seen in Fig. 4b. After cooling and freezing have completed after about 10^8 s or 3 years (c.f. Fig. 3), intrusion-parallel tensile stresses may still be present within the intrusion at about 160 MPa and within the ambient rock at about 20 MPa due to incomplete visco-elastic relaxation.

We also examined the stress evolution of a dyke emplaced at shallower depth (Case 2). The corresponding Figure is presented and discussed in more detail in the Supplementary information S4. Several differences to the hotter Case 1 are found: Heating of the colder wall rock leads to stronger compressive stresses of the order -200 MPa penetrating into the wall rock, followed by smaller tensile stresses upon cooling. As the amount of melting in the wall rock is very low (Fig. 3d), the effect of ambient rock melting on the stress evolution is almost negligible: only a short freezing event at around 10^7 s generates a peak of tensile stresses within a short distance to the dyke. Intrusion-parallel tensile stresses in the sill/dyke occur later compared to Case 1. As the sill/dyke cools and continues to solidify, strong tensile stresses develop and increase to 400 MPa at ca. 10 years. The low background temperatures lead to high viscosities and associated long Maxwell times up to $2 \cdot 10^{13}$ s (0.7 Ma) so that the stresses do not relax on this timescale. Given the shallower emplacement depth with about 330 MPa ambient lithostatic compressive stress and a tensile stress of about 400 MPa within the dyke due to solidification and cooling the total dyke parallel stress is tensile with a magnitude of about 70 MPa, while the dyke orthogonal stress is still compressive with 330 MPa.

4.3. Undrained pore pressure and expected melt flow

For Case 1) with significant melting it is interesting to evaluate the possible melt pressure. Given the stress field within and outside the intrusion, the total pressure is given by eq. (12). As discussed in section 3.3 the Skempton coefficient B can be determined within the partially molten regions to determine the instantaneous, undrained melt pressure $P_f = B P$. While this pressure will equilibrate with time and pressure diffusion (see section 3.3), its undrained distribution can still be used to get an idea about the maximum magnitude and the direction of porous melt flow. Fig. 5 shows the fluid pressure distribution. Note that for deep sill or dyke emplacement the ambient lithostatic pressure has to be added to this dynamic fluid pressure.

From Fig. 5 it can be seen, that within the partially melting regions within the ambient rock an over-pressure of up to 30 MPa will occur in Case 1 during about 10^3 to 10^6 s. Left of that region the melt fraction is above the RCMP and it is expected that the melt will be expelled into the high melt porosity region (arrows pointing to the left between 10^4 and 10^6 s). At the same time, within the partially molten region a negative pressure gradient is directed away from the intrusion (arrows pointing to the right). Once the ambient rock cools and the melt fraction drops below the RCMP, a strong negative pressure gradient develops from the

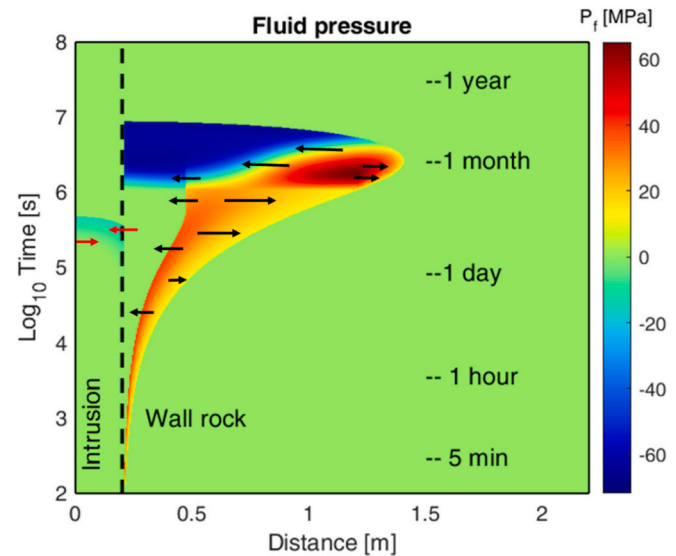


Fig. 5. Distribution of the undrained, non-lithostatic melt pressure for Case 1. In regions without melt the pressure is set to 0. In regions with high melt percentages above the RCMP the melt pressure is zero because the stresses are zero due to an open boundary condition at infinity x-direction. The arrows show the directions of decreasing pressure gradients, i.e. the directions of expected porous melt flow.

red to the blue region (10^6 – 10^7 s). During a short interval between $2 \cdot 10^6$ – $6 \cdot 10^7$ s the intrusion drops below the RCMP and an under-pressure develops (light blue area within the intrusion). The pressure is highest at the center of the intrusion and decreases towards the contact zone (red arrow at the center of the sill), indicating that melt is driven from the center towards the contact zone. A similar pressure gradient has already been proposed by Aarnes et al. (2009) based on a simpler model. As the high melt fraction region outside is at pressure 0 (or ambient lithostatic pressure) the more silicic melt of the ambient rock is expected to be sucked into the mafic intrusion (red arrow at the contact zone). The amount of melt within the sill was close to zero at this time (Fig. 3b), and increasing intrusion-parallel tensile stresses (ca. 40 MPa, Fig. 4a) might have led to tensile fractures (see next section) that were filled with the felsic melt. The tensile strength of mafic igneous rocks is generally < 40 MPa. Thus, here we derived a quantitative verification of the observed Sederholm effect (Zulauf et al., 2021).

5. Discussion

5.1. Brittle failure

In this section, we include the lithostatic stress at ambient conditions and test whether the total stresses within the intrusion or wall rock exceed the brittle strength.

We use the tectonic notation for normal and principal stresses, with compression positive and use the prime ' to denote these stresses (see Table 1). Thus, the intrusion parallel tectonic stress within or outside of the intrusion is given by $\sigma'_{\parallel} = -\sigma_{\parallel}$. Furthermore, the principal stresses are ordered as $\sigma'_1 \geq \sigma'_2 \geq \sigma'_3$ and the lithostatic stress is denoted as σ'_0 . Using the density of the ambient rock (Table 1) and a gravitational acceleration of 10 m s^{-2} , the lithostatic stresses in Case 1 at 15 km depth and in Case 2 at 10 km depth are approximately 420 MPa and 280 MPa, respectively. In case of a tensile intrusion parallel stress, $\sigma'_{\parallel} \leq 0$, and as the stress in orthogonal direction is zero, $\sigma'_{\perp} = -\sigma_{\perp} = 0$ (see section 2.2), we have the total principal tectonic stresses

$$\sigma'_3 = \sigma'_0 + \sigma'_{\parallel} \quad \text{and} \quad \sigma'_1 = \sigma'_0 \quad (16)$$

In case of a compressive intrusion parallel stress, $\sigma'_{\parallel} \geq 0$, and we

have

$$\sigma'_1 = \sigma'_0 + \sigma'_{\parallel} \quad \text{and} \quad \sigma'_3 = \sigma'_0 \quad (17)$$

We use these stresses to determine Mohr circles within a Mohr diagram, in which σ'_N is the normal stress on a plane of certain angle with respect to the first principal stress, and the ordinate gives the shear (tangential) stress σ'_T on that plane. We take the intrusion parallel stresses of cases 1 and 2 within and outside of the intrusions as shown in Figs. 4b and S3b (Supporting information). Separating them into different stages, eqs. (16 or 17) are taken to construct Mohr circles (black and blue) for these stages as denoted by the times given near the circles in Fig. 6. Additionally, the brittle strengths of diabase representing the intrusion (Fig. 6a and b), and of granodiorite and granite as possible rock types of the wall rock (Fig. 6c and d) are included. Mohr circles with a fixed point on the right side of the circle (e.g. black and blue circles in Fig. 6a, b) represent cases in which σ'_1 is fixed, as this stress represents the constant intrusion orthogonal stress. In this case, the intrusion parallel stress is less compressive than the lithostatic stress or even tensile if negative (Fig. 6b, large blue circles). In the wall rock at early stages (Fig. 6c and d) the left side of the black Mohr circles are fixed, representing σ'_3 as constant intrusion orthogonal stress, and the intrusion parallel stress is larger, i.e. more compressive than the lithostatic stress. Clearly, in the wall rock (Fig. 6c and d) the shear stresses

always remain below the strength envelopes, no brittle failure is predicted (blue and black Mohr circles). While the same is true for the intrusion of Case 1 (black, blue Mohr circles in Fig. 6a), the tensile stresses in the shallower intrusion of Case 2 (Fig. 6b, blue circles) may become very large at late stages due to cooler ambient temperatures and stronger thermal contraction. The brittle strength is exceeded at these stages predicting tensile shrinkage cracks. At these times, no more melt is present anymore to be sucked into the cracks.

Eqs. (16, 17) do not include the possible effect of fluid pressure P_{fior} . The melts in partially molten rock are pressurized and reduce the effective stresses. In this case, eqs. (16 and 17) can be written in terms of effective stresses:

$$\sigma'_{3eff} = \sigma'_0 + \sigma'_{\parallel} - P_{fior} \quad \text{and} \quad \sigma'_{1eff} = \sigma'_0 - P_{fior} \quad (18)$$

and for the case of a compressive intrusion parallel stress,

$$\sigma'_{1eff} = \sigma'_0 + \sigma'_{\parallel} - P_{fior} \quad \text{and} \quad \sigma'_{3eff} = \sigma'_0 - P_{fior} \quad (19)$$

As long as the melt fractions are above the RCMP, at least somewhere, we argued in section 2.4 that due to high connectivity of the melt, the melt pressure equilibrates at a value equal to the ambient lithostatic pressure, i.e. $P_{fior} = \sigma'_0$. In case of melt fractions below the RCMP we assume that the total pressure additionally includes the fluid pressure due to solidifying stresses (section 2.4), i.e. $P_{fior} = \sigma'_0 + P_f$. We

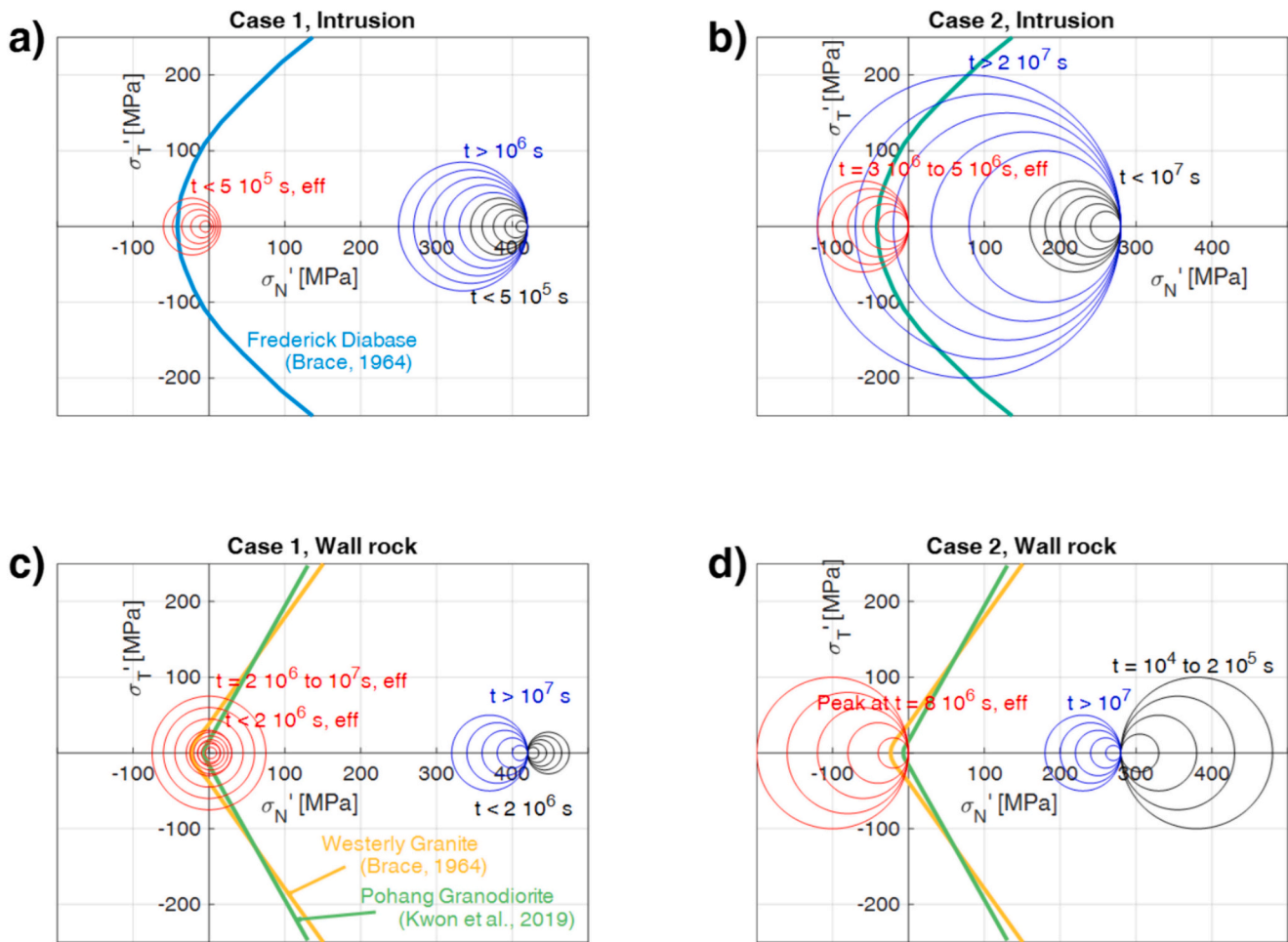


Fig. 6. Mohr diagrams for both Cases 1 and 2 within the intrusions and the wall rocks as denoted by the figure titles. Sets of principal stresses have been taken from Figs. 4b and S3b (Supporting information) for the stages indicated by the times denoted near the Mohr circles. The lithostatic stress at 15 km (Case 1) and 10 km (Case 2) has been added (eq. 16, 17) to the principal stresses to construct Mohr circles in a shear stress vs. normal stress Mohr diagram. In the presence of melt, the effective stresses are taken by using eq. (18, 19) assuming that the pore pressure of the melt is equal to the lithostatic pressure plus the solidification induced fluid pressure (see section 4.3). Strength envelopes of Diabase, Westerly Granite and Granodiorite are included (Brace, 1964; Kwon et al., 2019). If the Mohr circles exceed a strength envelope, tensile fracturing is predicted.

plot the corresponding Mohr circles for these stages when melt is present as red circles in Fig. 6. The circles are shifted towards and into the tensile regimes, exceeding the brittle strength envelopes in all cases in both the intrusion and wall rock. Tensile cracks are predicted. After complete freezing, no fluid pressure reduces the stress anymore and the Mohr circles are shifted back to the positions shown by the blue circles.

A few words about the chilled margins in Case 2. As they are below solidus, they do not contain any melt. For the stress within these margins, the concept of effective stress does not apply. The margins are represented by the black Mohr circles for times $<10^7$ s (Fig. 6b). At these times, melt is only present within the intrusion except the chilled margin, and within the wall rock. The chilled margin serves as a non-fractured impermeable barrier. Only at later stages ($>2 \cdot 10^7$ s) the stresses within the intrusion exceed the brittle strength (blue circles in Fig. 6b). At these stages no more melt is present anymore. Therefore, we conclude that as long as melt is present within the dyke or ambient rock, the chilled margin is not fractured and serves as an impermeable layer between the melt in the dyke and later, the small amounts of melt within the wall rock. No Sederholm-type melt filled fracturing is possible.

In summary, cooling and solidification of a mafic sill within a felsic wall rock generates visco-elastic effective stresses, which exceed the tensile strength of the mafic sill. Tensile strength within the cooling and solidifying felsic rock is only exceeded in the presence of pressurized felsic melts. If no other tectonic stresses are present, the two principal tensile stresses within and parallel to the dyke or sill are equal. Thus, if the tensile strength is exceeded in this particular case of axial-symmetric stress, the orientation of tensile cracks in three dimensions is arbitrary, i. e. tablet boudinage crack patterns as observed by Zulauf et al. (2011a, 2011b) or hexagonal patterns (Müller, 1998) are to be expected.

In the previous discussion, we did not consider the stresses associated with the dyke propagation nor emplacement of the intrusion. Dyke propagation is controlled by the ambient tectonic stress field, which we may refer to as background stress. Typical magnitudes are of the order 10 to 100 MPa (e.g. Turcotte and Schubert, 2002). Generally, dykes propagate in the direction of maximum compressive stress with the least compressive stress orthogonal to the dyke. Assuming that such a background stress is still present after emplacement, we may examine its interaction with the thermal or solidification/melting induced stresses. Within the intrusion these stresses or the Mohr circles of Fig. 6a, b are not affected by the background stress because prior to solidification the stress is isotropic. However, within the wall rock the background stress will superimpose with the thermal stresses. In the first phase of heating ($t < 10^6$ s, black and small orange circles in Fig. 6c, d), the thermal and background stresses superimpose constructively and the radii of the Mohr circles will increase, but the blue and black circles probably do not reach the strength envelopes. In the second phase ($t > 10^6$ s, blue and some of the orange circles) they interact with opposite signs. The Mohr circles will be reduced down to Mohr circles representing the background stress. Similar arguments may be derived with other kinds of additional ambient stresses, e.g. generated by the emplacement of an over-pressurized magma intrusion into an elastic medium.

5.2. Timescales, Deborah number

While our problem has been defined by two specific intrusion setups (Case 1 and 2), it is desirable to generalize some of the results. Whether a cooling and solidifying sill behaves elastically and large stresses will build up, or whether the stresses rapidly relax due to visco-elastic relaxation of the viscous rock depends on two timescales. These are the visco-elastic Maxwell time (eq. 14) and the thermal diffusion time

$$t_{diff} = \frac{h_i^2}{4\kappa_{eff}} \quad (20)$$

In eq. (20) we assumed that the characteristic diffusion length is equal to the half width of the intrusion, $h_i/2$, and the effective thermal

diffusivity is defined as $\kappa_{eff} = \frac{k}{\rho c_{p,eff}}$ with the effective heat capacity given by eq. (3). Generally the transition between elastic and viscous regimes can be described by the Deborah number,

$$De = \frac{t_{max}}{t_{proc}} \quad (21)$$

where t_{proc} is the characteristic time of the process or experiment under consideration. If $De < 1$, the material behaves essentially viscously, and stresses are relaxed. If $De > 1$ we have elastic behavior, and stresses are unrelaxed. In our case t_{proc} is the thermal diffusion time of cooling including solidification, thus using eq. (14) and (20) we have

$$De_{cool} = \frac{24\kappa_{eff}\eta_s(1-\nu)}{h_i^2 E \left(1 + \frac{4}{3} \frac{\eta_s}{\eta_b}\right)} \cong \frac{24\kappa_{eff}\eta_s(1-\nu)}{h_i^2 E} \quad (22)$$

where the approximation on the right hand side is valid for melt fractions well below the RCMP. The cooling Deborah number depends essentially on intrusion widths and rock viscosities. In general, at small width De_{cool} strongly increases to values above 1, but at lower viscosities De_{cool} will drop. This means that stresses within the intrusion or wall rock are still unrelaxed for narrow intrusions during the cooling process. They relax at times much later than the intrusion cools completely. Stresses in wider intrusions relax faster than the intrusion cools, i.e. they are already relaxed during the cooling process. It is interesting that these two effects are competitive in our Cases 1 and 2. The cooling Deborah numbers of both cases are well above 1 (i.e. unrelaxed) except for the wall rock of Case 2, where the width-effect dominates, leading to at least some relaxed stresses in the shallower wall rock. A detailed discussion with a regime diagram is given in the Supporting information (S4).

5.3. Comparison to natural dykes and sills

The model presented above has implications for the interpretation of natural igneous sheets. The presence of Sederholm-type shrinkage cracks filled with wall-rock derived melt is clear evidence for melt emplacement at deep structural levels where the wall rock is relatively hot. Such a structure is portrayed by the mafic sill in the Weschnitz pluton (Zulauf et al., 2021) that has been modelled as Case 1 where most of the critical parameters required for the modelling are well constrained. Further natural examples of Sederholm-type mafic sheets are described in the literature (e.g. Sederholm, 1912; Wyborn, n.d.; Skinner, 1983; Litvinovsky et al., 2012; Gatsenko and Kryvdik, 2018). In Case 1, the sill-parallel tensile stresses in the wall rock are large during the solidification phase until the wall rock attains its initial temperature and melt is negligible or absent. During this short period, tensile fractures might have opened (c.f. red Mohr circles in Fig. 6c), which formed possible weak zones during subsequent mullion formation (see Figs. 9 and 15 in Zulauf et al., 2022). The cusps of these mullions might have developed preferably along these pre-existing fractures.

It is further obvious from the modelling results of Case 1 that elevated pore-fluid pressure is important for the transport of melt from the wall rock into the shrinkage cracks of the sill. Moreover, at such deep structural levels, elevated pore-fluid pressure in addition to low differential stress (in our case $\sigma'_1 - \sigma'_3$) are main prerequisites to open the subhorizontal vein along which the mafic melt has emplaced as sill (Secor, 1965).

Because of the low temperature of the wall rock, partial melting of the wall rock does not play a significant role at upper structural levels. For this reason, possible shrinkage cracks are not filled with wall-rock derived melt. Such a structure is portrayed by the younger dyke, which cuts through the Weschnitz pluton and has been modelled as Case 2. There are numerous examples of such shallow dykes described in the literature and in textbooks. It should be emphasized, however, that felsic melts in shrinkage cracks of mafic dikes are not entirely excluded in the

upper crust. In cases of multiple injections of mafic melt at the same orientation in the sheet, partial melting of the wall rock is possible although the wall-rock temperature is low (Petkovic and Grunder, 2003; Petkovic and Dufek, 2005).

Apart from dyke-orthogonal joints, there are also joints aligned parallel to the dyke of Case 2 (Fig. 1c). A further example is shown in Fig. 1f. As dyke orthogonal tensile stresses are not predicted by cooling and solidifying of a planar intrusion (no tensile stresses inside the intrusions in Figs. 4a,b, S3a,b, Supporting information), the stresses in the dyke must have changed probably due to changes of the bulk tectonic stress field. Note, that the opening of the NNE-SSW trending dyke in Case 2 was related to a tensile stress (σ'_3) in the WNW-ESE direction. After the dyke had formed and cooled, this tensile stress might have built up again exceeding the tensile strength of the dyke and resulting in the dyke-parallel joints.

The modelling results have also implications for the formation of chilled margins. A chilled margin develops because the heat flux from the melt cannot balance the very large initial conductive flux in the rock (Huppert and Sparks, 1989). From the modelling of the mafic sill in Case 1, it is shown that chilled margins cannot form at deep structural levels because immediately after melt emplacement, the temperature at the sheet/wall rock contact was still above the solidus of the mafic melt. In Case 2, on the other hand, the temperature at the contact between dyke and wall rock was below the solidus of the mafic melt and formation of a chilled margin was possible. This chilled margin would be even more pronounced if the melt were emplaced at even shallower structural levels, where the difference between melt and wall rock was larger. Such well-developed chilled margins, however, can be overprinted not only in cases of multiple melt emplacement as described from the large Steinmauer dyke in the Weschnitz pluton (Nickel and Fettel, 1985) or from other dykes described above, but also after single-phase melt emplacement if the conductive heat flux is exceeded by the heat flux from the melt. In these circumstances, the chilled margin begins to remelt and can even disappear (Huppert and Sparks, 1989).

5.4. Limitations of the models

As all sill and dyke models published so far, the model presented here has several limitations. These are discussed in detail in the supporting information (S5).

6. Conclusions

Using two parameters sets of a deep (Case 1, 15 km) and shallower (Case 2, 10 km) planar intrusion with ambient temperatures of 650 °C and 400 °C, respectively, the evolution of melting, solidification, temperature, and stress-field including visco-elastic relaxation has been modelled. The two cases are based on field observations from the Weschnitz pluton (Odenwald). While in Case 1 extensive melting of the wall rock occurs, in Case 2 the margin of the intrusion immediately freezes because the contact temperature is 75 °C below the solidus temperature of the mafic melt. A chilled margin forms. Small amounts of wall rock melting are observed, but the impermeable chilled margin inhibits melt exchange between the intrusion and the wall rock.

Assuming a visco-elastic Maxwell rheology with temperature- and melt fraction dependent non-Newtonian rock viscosity and melt fraction dependent elasticity, the intrusion-parallel stress σ_{\parallel} has been numerically determined. The intrusion orthogonal stress σ_{\perp} is always zero. As long as melt fractions are above the RCMP, σ_{\parallel} within the partially molten intrusion or wall rock is zero. During solidification at lower melt fractions and subsequent cooling, σ_{\parallel} strongly increase with the following results:

- σ_{\parallel} within the intrusion is found to be tensile, increasing to about 150 MPa (Case 1) or 400 MPa (Case 2), and then relaxing on a time scale of a few years (Case 1) or 0.6 Ma (Case 2).
- Within the wall rock during the heating phase σ_{\parallel} is compressive (−50 MPa in Case 1, −250 MPa in Case 2), but becomes tensile during the cooling phase (150 MPa in Case 1, 100 MPa in Case 2). Wall rock stresses relax on a time scale of months to years (Case 1) or years to 100 years (Case 2).
- To generalize the visco-elastic behavior, a Deborah number has been defined as the ratio of the Maxwell time to the diffusive cooling time. In both cases the Deborah number is well above 1, except for early periods within the wall rock in Case 2.
- Fluid pressure within the melt has been determined in Case 1: During melting of the wall rock an over-pressure develops. During solidification of the intrusion and, later, of the wall rock, the melt pressure is negative. The resulting pressure gradients suggest that felsic melts are driven towards, and sucked into the dyke, and that mafic melts are driven from the dyke center towards the contact zone.
- Adding lithostatic compressive stresses to the cooling/solidifying stresses, the total stresses of the deeper Case 1 are always below the brittle strength envelope. For the shallower Case 2 the intrusion stresses may exceed the brittle tensile strength, while in the wall rock it remains below the brittle strength. Only if the lithostatic pressure is added to the melt pressure, the effective stresses exceed the brittle strength in both cases, and tensile Sederholm-type fracturing is predicted for Case 1.
- The combination of fracture predictions and over-pressurized felsic melts explain the transport of melt from the wall rock into the shrinkage cracks of the sill in the Weschnitz pluton. The presence of the impermeable chilled margin in Case 2 in the presence of melt within the dyke or ambient rock explains that no felsic melt is found within the shallower dyke. Tensile fracturing of the dyke only starts when all melt is solidified.

CRediT authorship contribution statement

Harro Schmeling: Writing – original draft, Visualization, Validation, Software, Methodology, Investigation, Funding acquisition, Formal analysis, Conceptualization. **Gernold Zulauf:** Writing – review & editing, Writing – original draft, Validation, Methodology, Investigation, Conceptualization.

Declaration of competing interest

The authors declare that they have no known competing financial interests or personal relationships that could have appeared to influence the work reported in this paper.

Data availability.

The data of this paper consist of modelling results generated by the own developed codes using MATLAB. These codes including some input and output data are available at [https://user.uni-frankfurt.de/~schmelin/***\(for the review process; will be available on Zenodo after acceptance\).](https://user.uni-frankfurt.de/~schmelin/***(for the review process; will be available on Zenodo after acceptance).)

Data availability

Data will be made available on request.

Acknowledgements

Inspired by G. Z. during a visit at the Weschnitz pluton, H.S. developed the visco-elastic formulation. H.S. is grateful to B. Kaus and G. Golabek for organizing the “Harro-Schmeling-Symposium” in September 2020, on which the first results of this paper have been presented. The research has been supported by the Deutsche Forschungsgemeinschaft (grant no. SCHM 872/28-1).

Appendix A. Supplementary data

Supplementary data to this article can be found online at <https://doi.org/10.1016/j.tecto.2024.230367>.

References

- Aarnes, I., Podlachikov, Y.Y., Neumann, E.-R., 2009. Post-emplacement melt flow induced by thermal stresses: Implications for differentiation in sills, *Earth Planet. Sci. Lett.* 276, 152–166. <https://doi.org/10.1016/j.epsl.2008.09.016>.
- Altherr, R., Henes-Klaiber, U., Hegner, E., Satir, M., Langer, C., 1999. Plutonism in the Variscan Odenwald (Germany): from subduction to collision. *Int. J. Earth Sci.* 88, 422–443.
- Annen, C., 2017. Factors affecting the thickness of thermal aureoles. *Front. Earth Sci.* 5, 82. <https://doi.org/10.3389/feart.2017.00082>.
- Annen, C., Blundy, D., Sparks, R.S.J., 2006. The genesis of intermediate and silicic magmas in deep crustal hot zones. *J. Petrol.* 47, 505–539.
- Annen, C., Pichavant, M., Bachmann, O., Burgisser, A., 2008. Conditions for the growth of a long-lived shallow crustal magma chamber below Mount Pelee volcano (Martinique, Lesser Antilles Arc). *J. Geophys. Res.* 113, B07209. <https://doi.org/10.1029/2007JB005049>.
- Arzi, A.A., 1978. Critical phenomena in the rheology of partially melted rocks. *Tectonophysics* 44, 173–184.
- Bagdassarov, N., 2022. *Fundamentals of Rock Physics*. Cambridge University Press, Cambridge. <https://doi.org/10.1017/9781108380713>.
- Barnett, Z.A., Gudmundsson, A., 2014. Numerical modelling of dykes deflected into sills to form a magma chamber. *J. Volcanol. Geotherm. Res.* 281, 1–11 dx.doi.org/. <https://doi.org/10.1016/j.jvolgeores.2014.05.018>.
- Bazargan, M., Gudmundsson, A., 2019. Dike-induced stresses and displacements in layered volcanic zones. *J. Volcanol. Geotherm. Res.* 384, 189–205. <https://doi.org/10.1016/j.jvolgeores.2019.07.010>.
- Brace, W.F., 1964. 1964. Brittle fracture of rocks. In: Judd, W.R. (Ed.), *State of Stress in the Earth's Crust*. American Elsevier Publishing Company, New York, pp. 110–178.
- Browning, J., Meredith, P., Gudmundsson, A., 2016. Cooling-dominated cracking in thermally stressed volcanic rocks. *Geophys. Res. Lett.* 43, 8417–8425. <https://doi.org/10.1002/2016GL070532>.
- Browning, J., Karaoglu, Ö., Bayer, Ö., Turgay, M.B., Acocella, V., 2021. Stress fields around magma chambers influenced by elastic thermo-mechanical deformation: implications for forecasting chamber failure. *Bull. Volcanol.* 83, 48. <https://doi.org/10.1007/s00445-021-01471-2>.
- Carracedo, J.C., Troll, V.R., 2016. *The Geology of the Canary Islands*. Elsevier, Amsterdam.
- Costa, F., Scaillet, B., Pichavant, M., 2004. Petrological and experimental constraints on the pre-eruption conditions of Holocene dacite from Volcán San Pedro (36°S, Chilean Andes) and the importance of Sulphur in silicic subduction-related magmas. *J. Petrol.* 45, 855–884.
- Dahm, T., 2000. Numerical simulations of the propagation path and the arrest of fluid-filled fractures in the Earth. *Geophys. J. Int.* 141, 623–638.
- Delany, P.T., Pollard, D.D., 1982. Solidification of basaltic magma during flow in a dike. *Amer. J. Sci.* 282, 856–885.
- Drymoni, K., Browning, J., Gudmundsson, A., 2020. Dyke-arrest scenarios in extensional regimes: Insights from field observations and numerical models, Santorini, Greece. *J. Volcanol. Geotherm. Res.* 396, 106854 <https://doi.org/10.1016/j.jvolgeores.2020.106854>.
- Dufek, J., Bergantz, G.W., 2005. Lower Crustal Magma Genesis and Preservation: a Stochastic Framework for the Evaluation of Basalt–Crust Interaction. *J. Petrol.* 46, 2167–2195. <https://doi.org/10.1093/petrology/egi049>.
- Eshelby, J.D., 1957. The determination of the elastic field of an ellipsoidal inclusion, and related problems, *Proceedings of the royal society of London. Series a. Mathe. phys. sci.* 241 (1226), 376–396.
- Eskola, P., 1960. Granitenstehung bei Orogenese und Epirogenese. *Geol. Rundsch.* 50, 105–123.
- Gatsenko, V.O., Kryvdik, S.G., 2018. The Sederholm effect in dykes of the Pokrovo-Kyryivovo Massif (Azov Area, Ukraine). *Геол. та палеон. 39*, 108–114. <https://doi.org/10.15407/gof.2018.39.108> (in Russian with English abstract).
- Gudmundsson, A., 1990. Emplacement of dikes, sills and crustal magma chambers at divergent plate boundaries. *Tectonophysics* 176, 257–275.
- Gudmundsson, A., 2006. How local stresses control magma-chamber ruptures, dyke injections, and eruptions in composite volcanoes, *Earth Sci. Rev.* 79, 1–31. <https://doi.org/10.1016/j.earscirev.2006.06.006>.
- Harrison, T.M., 1981. Diffusion of ⁴⁰Ar in hornblende. *Contrib. Mineral. Petrol.* 78, 324–331.
- Harrison, T.M., Duncan, I., McDougall, I., 1985. Diffusion of ⁴⁰Ar in biotite: Temperature, pressure and compositional effects. *Geochim. Cosmochim. Acta* 49, 2461–2468.
- Head, M., Hickey, J., Gottsmann, J., Fournier, N., 2019. The influence of viscoelastic crustal rheologies on volcanic ground deformation: Insights from models of pressure and volume change. *J. Geophys. Res.* 124, 8127–8146. <https://doi.org/10.1029/2019JB017832>.
- Hickey, J., Gottsmann, J., del Potro, R., 2013. The large-scale surface uplift in the Altiplano-Puna region of Bolivia: a parametric study of source characteristics and crustal rheology using finite element analysis. *Geochim. Geophys. Res.* 14, 540–555. <https://doi.org/10.1002/ggge.20057>.
- Hickey, J., Gottsmann, J., Nakamichi, H., Iguchi, M., 2016. Thermomechanical controls on magma supply and volcanic deformation: application to Aira caldera. *Japan. Sci. Rep.* 6, 32691. <https://doi.org/10.1038/srep32691>.
- Huppert, H.E., Sparks, R.S.J., 1989. Chilled margins in igneous rocks. *Earth Planet. Sci. Lett.* 397–405.
- Irvine, T.N., 1970. Heat transfer during solidification of layered intrusions. I. Sheets and sills. *Can. J. Earth Sci.* 7, 1031–1061. <https://doi.org/10.1139/e70-098>.
- Jaeger, J.C., 1957. The temperature in the neighborhood of a cooling intrusive sheet. *Amer. J. Sci.* 255, 306–318. <https://doi.org/10.2475/ajs.255.4.306>.
- Jellinek, A.M., DePaolo, D.J., 2003. A model for the origin of large silicic magma chambers: precursors of caldera-forming eruptions. *Bull. Volcanol.* 65, 363–381.
- Karakas, O., Dufek, J., 2015. Melt evolution and residence in extending crust: thermal modeling of the crust and crustal magmas, *Earth Planet. Sci. Lett.* 425, 131–144. <https://doi.org/10.1016/j.epsl.2015.06.001>.
- Karlstrom, L., Dufek, J., Manga, M., 2009. Organization of volcanic plumbing through magmatic lensing by magma chambers and volcanic loads. *J. Geophys. Res.* 114, B10204. <https://doi.org/10.1029/2009JB006339>.
- Karlstrom, L., Dufek, J., Manga, M., 2010. Magma chamber stability in arc and continental crust. *J. Volcanol. Geotherm. Res.* 190, 249–270. <https://doi.org/10.1016/j.jvolgeores.2009.10.003>.
- Karlstrom, L., Paterson, S.R., Jellinek, A.M., 2017. A reverse energy cascade for crustal magma transport. *Nat. Geosci.* 10, 604–608. <https://doi.org/10.1038/ngeo2982>.
- Kirby, S.H., Kronenberg, A.K., 1987. Correction to “Rheology of the lithosphere: selected topics”. *Rev. Geophys.* 25, 1680–1681.
- Kreuzer, H., Harre, W., 1975. K/Ar-Altersbestimmungen an Hornblenden und Biotiten des Kristallinen Odenwaldes. In: Amstutz, G.C., Meisl, S., Nickel, E. (ed.): *Mineralien und Gesteine im Odenwald. Aufschluß, Sonderband 27*, 71–77.
- Kwon, S., Xie, L., Park, S., Kim, K.-I., Min, K.-B., Kim, K.Y., Zhuang, L., Choi, J., Kim, H., Lee, T.-J., 2019. Characterization of 4.2-km-Deep Fractured Granodiorite Cores from Pohang Geothermal Reservoir. *Korea, Rock Mech. Rock Eng.* 52, 771–782. <https://doi.org/10.1007/s00603-018-1639-2>.
- Lambert, I.B., Wyllie, P.J., 1972. Melting of Gabbro (Quartz Eclogite) with Excess Water to 35 Kilobars, with Geological applications. *J. Geol.* 80, 693–708.
- Liao, Y., Karlstrom, L., Erickson, B.A., 2023. History-dependent volcanic ground deformation from broad-spectrum viscoelastic rheology around magma reservoirs, *Geophys. Res. Lett.* 50. <https://doi.org/10.1029/2022GL101172>.
- Litvinovsky, B.A., Zanzvilevich, A.N., Kätzir, Y., 2012. Formation of composite dikes by contact remelting and magma mingling: the Shaluta pluton, Transbaikalia (Russia). *J. Asian Earth Sci.* 60, 18–30.
- Litvinovsky, B.A., Zanzvilevich, A.N., Wickham, S.M., Jahn, B.M., Vapnik, Y., Kanakin, S. V., Karmanov, N.S., 2017. Composite dikes in four successive granitoid suites from Transbaikalia, Russia: the effect of silicic and mafic magma interaction on the chemical features of granitoids. *J. Asian Earth Sci.* 136, 16–39.
- Maccaferri, F., Smittarello, D., Pinel, V., Cayol, V., 2019. On the propagation path of magma-filled dikes and hydrofractures: the competition between external stress, internal pressure, and crack length. *Geochim. Geophys. Res.* 20 <https://doi.org/10.1029/2018GC007915>.
- Moore, G., Carmichael, I.S.E., 1998. The hydrous phase equilibria (to 3 kbar) of an andesite and basaltic andesite from western Mexico: constraints on water content and conditions of phenocryst growth. *Contrib. Mineral. Petrol.* 130, 304–319.
- Müller, G., 1998. Starch columns: Analog model for basalt columns. *J. Geophys. Res.* 103 <https://doi.org/10.1029/98JB00389>, 15 239–15 252.
- Nickel, E., Fettel, M., 1985. Odenwald. In: *Vorderer Odenwald zwischen Darmstadt und Heidelberg, Sammlung Geologischer Führer, Volume 65*. Gebrüder Borntraeger, Berlin.
- Petecovic, H.L., Dufek, J.D., 2005. Modeling magma flow and cooling in dikes: Implications for emplacement of Columbia River flood basalts. *J. Geophys. Res.* 110, B10201. <https://doi.org/10.1029/2004JB003432>.
- Petecovic, H.L., Grunder, A.L., 2003. Textural and thermal history of partial melting in tonalitic walkrock at the margin of a basalt dike, Wallowa Mountains, Oregon. *J. Petrol.* 44, 2287–2312.
- Pinel, V., Jaupart, C., 2003. Magma chamber behavior beneath a volcanic edifice. *J. Geophys. Res.* 108 (B2) <https://doi.org/10.1029/2002JB001751>.
- Rittmann, K.L., 1984. Argon in Hornblende, Biotit und Muskovit bei der geologischen Abkühlung - ⁴⁰Ar/³⁹Ar-Untersuchungen, PHD thesis. University of Heidelberg, p. 278 (unpublished).
- Rivalta, E., Taisne, B., Buger, A.P., Katz, R.F., 2015. A review of mechanical models of dike propagation: schools of thought, results and future directions. *Tectonophysics* 638, 1–42.
- Rosenberg, C.L., Handy, M.R., 2005. Experimental deformation of partially melted granite revisited: implications for the continental crust. *J. Metamorph. Geol.* 23 (1), 19–28.
- Rucker, C., Erickson, B.A., Karlstrom, L., Lee, B., Gopalakrishnan, J., 2022. A computational framework for time-dependent deformation in viscoelastic magmatic systems. *J. Geophys. Res.* 127 <https://doi.org/10.1029/2022JB024506> e2022JB024506.
- Schmeling, H., 1985. Numerical models on the influence of partial melt on elastic, anelastic, and electric properties of rocks. Part I: elasticity and anelasticity. *Phys. Earth Planet. Inter.* 41, 34–57.
- Schmeling, H., Kruse, J.-P., Richard, G., 2012. Effective shear and bulk viscosity of partially molten rock based on elastic moduli theory of a fluid filled poroelastic medium. *Geophys. J. Int.* 190, 1571–1578. <https://doi.org/10.1111/j.1365-246X.2012.05596.x>.
- Secor, D.T., 1965. Role of fluid pressure in jointing. *Am. J. Sci.* 263, 633–646.
- Sederholm, J.J., 1907. Om granit och gneis, deras uppkomst, uppträdande och utbredning inom urberget i Fennoskandia. *Bull. Comm. géol. Finl.* No. p. 23.

- Sederholm, J.J., 1912. About palingenesis in the southern Funen archipelago and the division of Finnish Unberg. *Geol. För. Förb.* 34, 293 (p. [in Swedish]).
- Skinner, D.N.B., 1983. The Geology of Terra Nova Bay. In: Oliver, R.L., James, P.R., Jago, J.B. (Eds.), *Antarctic Earth Science*. Australian Academy of Science, Canberra, pp. 150–155.
- Solano, J.M.S., Jackson, M.D., Sparks, R.S.J., Blundy, J.D., Annen, C., 2012. Melt Segregation in Deep Crustal Hot zones: a Mechanism for Chemical Differentiation, Crustal Assimilation and the Formation of Evolved Magmas. *J. Petrol.* 53, 1999–2026. <https://doi.org/10.1093/petrology/egs041>.
- Suppe, J., 1983. *Principles of Structural Geology*, 537 pp., Prentice Hall, London.
- Townsend, M.R., Pollard, D.D., Smith, R.P., 2017. Mechanical models for dikes: a third school of thought. *Tectonophysics* 703, 98–118.
- Turcotte, D.L., Schubert, G., 2002. *Geodynamics*. John Wiley & Sons, New York.
- Von Seckendorff, V., Timmerman, M.J., Kramer, W., Wrobel, P., 2004. New ⁴⁰Ar/³⁹Ar ages and geochemistry of late Carboniferous-early Permian lamprophyres and related volcanic rocks in the Saxothuringian Zone of the Variscan Orogen (Germany). *Geol. Soc. Lond. Spec. Publ.* 223 (1), 335–359.
- Walker, G.P.L., 1974. The structure of eastern Iceland. In: Kristjansson, L. (Ed.), *Geodynamics of Iceland and the North Atlantic Area*, NATO Advanced Study Institutes Series V. 11. Springer, Dordrecht, pp. 177–188. https://doi.org/10.1007/978-94-010-2271-2_12.
- Weinberg, R.F., Vernon, R.H., Schmeling, H., 2021. Processes in mushes and their role in the differentiation of granitic rocks. *Earth Sci. Rev.* 220, 103665 <https://doi.org/10.1016/j.earscirev.2021.103665>.
- Wyborn, D., 1981. Granitoids of North Victoria Land, Antarctica – Field and Petrographic Observations. *Geol. Jb.* B41, 229–249. Hannover.
- Zulauf, G., Heflerich, S., 1997. Strain and strain rate in a synkinematic trondhjemitic dike: evidence for melt-induced strain softening during shearing (Bohemian Massif, Czech Republic). *J. Struct. Geol.* 19, 639–652.
- Zulauf, J., Zulauf, G., Kraus, R., Guitierrez-Alonso, G., Zanella, F., 2011a. The origin of tablet boudinage: results from experiments using power-law rock analogs. *Tectonophysics* 510, 327–336. <https://doi.org/10.1016/j.tecto.2011.07.013>.
- Zulauf, J., Zulauf, G., Hammer, J., Zanella, F., 2011b. Tablet boudinage of an anhydrite layer in rock-salt matrix: results from thermomechanical experiments. *J. Struct. Geol.* 33, 1801–1815. <https://doi.org/10.1016/j.jsg.2011.09.006>.
- Zulauf, G., Gerdes, A., Hattingen, E., Hoefler, H.E., Loeckle, F., Marschall, H.R., Nesbor, H.-D., Petschick, R., Reischmann, T., Schmeling, H., Zulauf, J., 2021. Development of a synorogenic composite sill at deep structural levels of a continental arc (Odenwald, Germany). Part 1: Sederholm-type emplacement portrayed by contact melt in shrinkage cracks. *Tectonophysics* 805, 228774. <https://doi.org/10.1016/j.tecto.2021.228774>.
- Zulauf, G., Zulauf, J., Linckens, J., Gerdes, A., Hattingen, E., Loeckle, F., Marschall, H.R., Steckenreiter, L., 2022. Development of a synorogenic composite sill at deep structural levels of a magmatic arc (Odenwald, Germany). Part 2: Rheological inversion and mullion formation under bulk constriction. *J. Struct. Geol.* 155 <https://doi.org/10.1016/j.jsg.2022.104525>.